Journal of Volcanology and Geothermal Research 467 (2025) 108416

Contents lists available at ScienceDirect

Journal of Volcanology and Geothermal Research

journal homepage: www.journals.elsevier.com/journal-of-volcanology-and-geothermal-research

Tracing the pre- to post-eruptive crystallization of trachybasaltic melts: insights into the 1651–1654 CE lavas of Mount Etna (Sicily, Italy)

G. Lanzafame [a], S. Peres [b], F. Casetta [b], R. Abart [b], M. Prašek [c,*], S. Portale [a,d], P.P. Giacomoni [e], E. Libowitzky [f], C. Ferlito [a]

[a] Department of Biological, Geological and Environmental Sciences, University of Catania, Corso Italia 57, 95129 Catania, Italy
[b] Department of Lithospheric Research, University of Vienna, Josef-Holaubek-Platz 2 (UZA II), 1090 Vienna, Austria
[c] Elettra Sincrotrone Trieste S.C.p.A., SS14 km 163.5 in Area Science Park, 34149 Basovizza, Italy
[d] Department of Human Sciences, University of Catania, Piazza Dante Alighieri 24, 95124 Catania, Italy
[e] Department of Earth Sciences, University of Pisa, Via S. Maria 53, 56126 Pisa, Italy
[f] Department of Mineralogy and Crystallography, University of Vienna, Josef-Holaubek-Platz 2 (UZA II), 1090 Vienna, Austria

ARTICLE INFO

Keywords:
Mount Etna volcano
Crystallization
Lava rheology
Trachybasaltic melts

ABSTRACT

Understanding the crystallization of silicate melts is key to reconstructing the processes occurring from magma rising to lava emplacement, the latter representing a major hazard for human settlements during effusive eruptions. Crystal growth, along with melt H_2O degassing, strongly influences lava rheology and surface flow behaviour. This study investigates the pre- to post-eruptive crystallization dynamics of trachybasaltic melts from the 1651–1654 CE eruption on Mount Etna's western flank (Sicily, Italy), one of the 17th century's most significant events due to its duration, lava field extent, and reach into inhabited areas. Investigation on different layers of a fractured pressure ridge allowed to reconstruct the crystallization history of a single flow unit, revealing significant textural differences between the inner and outer (crust) portion of the lava, allowing to quantify the extent of crystallization at subaerial conditions. By combining 2D and 3D textural analyses with chemical and mineralogical investigations, the pre-eruptive pressure-temperature (P–T) conditions of crystal formation were constrained. Phenocrysts nucleated in a vertically extended feeding system (down to 23 km below the sea level) at almost stationary condition of $T = 1070$–1060 °C. In the glass-rich crust, detailed chemical and textural analyses revealed chemical boundary layers around plagioclase microlites, which was used to model a subaerial growth rate of the outermost plagioclase rim in the order of 0.2–4.5 μm/s. These findings enhance our understanding of lava behaviour during flow, offering key insights for improving hazard models, monitoring, and response during effusive volcanic events similar to the 1651–1654 CE eruption.

1. Introduction

On active volcanoes characterized by frequent effusive eruptions, invasion by lava flows may lead to the disruption of inhabited regions, agricultural lands and industrial zones, posing a serious threat to both residential communities and economic infrastructures, representing one of the most significant hazards to human activities (Troll et al., 2024). The extent of lava flow propagation from its emission point depends on the interplay of many factors, including the amount of magma feeding the eruption and its emission rate, the slope morphology and the rheological properties of the lava, which depends on its viscosity. Viscosity is mainly a function of chemical, physical and textural properties such as composition, temperature, crystal cargo and vesicle content (Giordano et al., 2008; Vona et al., 2011; Mader et al., 2013; Kolzenburg et al., 2022; Namiki et al., 2025) and plays a fundamental role in determining the ability of a lava to flow (Calvari and Pinkerton, 1999; Lanzafame et al., 2022).

Once lava is erupted, complex and interacting processes contribute to its flow path on the surface. In fact, lava flows are in strong physical disequilibrium with the atmosphere and solidify at cooling rates driven by the temperature difference (ΔT) to the surrounding environment. During flow, ΔT decreases from the outer portions of the lava flow exposed to colder atmosphere and bedrock, towards the inner part where heat is more easily preserved. This often forms rigid lateral banks,

* Corresponding author.
E-mail address: marko.prasek@elettra.eu (M. Prašek).

https://doi.org/10.1016/j.jvolgeores.2025.108416
Received 23 May 2025; Received in revised form 1 August 2025; Accepted 2 August 2025
Available online 12 August 2025

which helps channel lava into well-defined paths. As the outer portions of the flow continue to cool, solidification can extend to the surface, forming a rigid outer crust and developing lava tubes that insulate the molten flow, reducing its ability to lose heat, thus keeping it at a relatively high temperature and low viscosity and allowing its travel for long distances (Calvari and Pinkerton, 1999; Lanzafame and Ferlito, 2014; Lanzafame et al., 2022). Understanding why (and if) effusive eruptions from a certain volcano are prone to the formation of lava tubes is of paramount importance for evaluating the volcanic hazard. Variation in the emission rate upstream or changes in the downstream topography determine the increase in pressure within the tubes, causing the lava to inflate and break its crust, eventually leading to its tilting outward, forming structures known as pressure ridge or tumuli (Walker, 1991; Hon et al., 1994; Anderson et al., 2012; Robert et al., 2014; Harris et al., 2022). When preserved, the breached portions of the outer crust of lava flows expose an accessible vertical section that allows the study of the different and outermost levels of the flow. Previous studies have demonstrated that variations in cooling rates can have a significant impact on both the texture and chemical composition of the solidified regions (Cashman, 1993; Mollo et al., 2011, 2012, 2013a, 2013b; Shea and Hammer, 2013; Giuliani et al., 2020).

In this work, we traced the evolution of a trachybasaltic melt from the initial nucleation of minerals under pre-eruptive conditions to its subaerial solidification as a lava flow. The study is based on a detailed petrologic characterization of a pressure ridge formed by fracturing and tilting of a flow unit of the pahoehoe lava field emplaced during the 1651–1654 CE eruption at Mount Etna (Fig. 1). Textural investigation by scanning electron microscopy (SEM) and phase-contrast synchrotron X-ray computed microtomography (SR X-μCT), coupled with mineral chemical analysis by electron probe microanalysis (EPMA) enabled for modelling the pre- and post-eruptive crystallization and degassing processes, and to reveal the profound effect that different cooling paths have on final texture of trachybasaltic lavas. Our results showed that the fast-crystallizing glass-rich crust and the inner massive portion of single flows are different from each other, both in their crystal cargo and mineral textures. The investigation of the microlites in the groundmass of the lava crust revealed the preservation of chemical boundary layers around plagioclase crystals and allowed us to quantify the growth rate of these crystals on the surface of the flow, shedding new light on the timescale of crystallization of lavas during their emplacement.

2. Mount Etna volcano and the 1651–1654 CE eruption

Located on the eastern coast of Sicily (Italy), Mount Etna is one of the most active volcanoes in the world. Its activity can be traced back to about 0.5 My ago. Since then, the volcano has gone through different evolutionary stages. The initial tholeiitic phase (~500–220 ky ago) was followed by transitional (220–110 ky ago) and Na-alkaline phases, the last one is responsible for the construction of distinct stratovolcanoes (~110–65 ky) the remnants of which crop out on the flanks of the 'Valle del Bove' depression located on the eastern flank of Mount Etna (Tanguy et al., 1997; de Beni et al., 2005; Branca et al., 2008; Catalano et al., 2004; Casetta et al., 2020). The present-day edifice reaches a height of ~3350 m above sea level (a.s.l.), covers an area of ~1400 km^2, and is built by the superposition of countless lava and tephra deposits formed during the latest activity, which started ~57 ky ago and is subdivided into Ancient (Ellittico) and Recent Mongibello phase (Monaco et al., 2010; Branca et al., 2011). The activity of the Recent Mongibello (~15 ky to present) is characterized by the occurrence of explosive and effusive eruptions of mostly hawaiitic to trachybasaltic products at the summit craters (central activity), along fissures opening on the volcano flanks (lateral eruptions), or even at large distances of up to tens of km from the volcano main craters (eccentric eruptions) (Rittmann, 1965; Andronico and Lodato, 2005; Andronico et al., 2005). The most impressive feature of Mount Etna is the persistent degassing from the summit craters, which testifies to an open conduit nature of its plumbing system from which thousands of tons of volatiles, mostly H_2O, CO_2 and SO_2, are daily emitted into the atmosphere (Ferlito et al., 2014; Ferlito et al., 2017; Aiuppa et al., 2021, 2023; La Spina et al., 2023).

In the historic period, several effusive events threatened human activity on all the flanks of the volcano due to the opening of eruptive fissures and the formation of monogenetic vents located at low altitude. These episodes often involved contemporaneous strombolian activity from newly grown scoria cones and emission of high amounts (in the order of 10^6–10^8 m^3) of lava. In this regard, the most intense period of activity was the 17th century, marked by three main eruptive phases on the northern (1614–1624 CE), western (1651–1654 CE) and southern (1669 CE) flanks of Mount Etna, during which lava flows with hawaiitic composition emitted by flank eruptions invaded low altitude populated areas, causing major damages to the human settlements (Branca and Abate, 2019). The lavas erupted during the 1614–1624 and 1651–1654 events represent an interesting case study for Mount Etna also because of their peculiar texture, given by the large size of plagioclase phenocrysts (>10 mm) which led to the local definition of "cicirara" lavas, referring

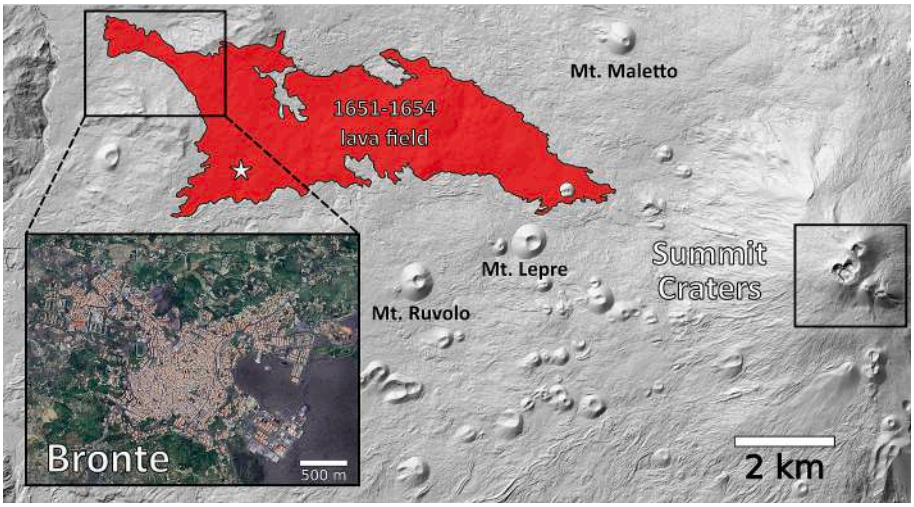

Fig. 1. Location of the main lava field of the 1651–1654 eruption on the western flank of Mount Etna volcano, where eruptive vents have been buried by subsequent activity. The inset shows the satellite view of the present-day area of Bronte town, partly built on the distal portion of the lava field. The star indicates the location of the sampled lava flow.

to the chickpeas like appearance of plagioclase phenocrysts (Lanzafame et al., 2013; Vetere et al., 2015). Previous studies by Lanzafame et al. (2013) and Vetere et al. (2015) on these lavas demonstrated that the nucleation of plagioclase initially started in a pre-eruptive environment, but plagioclase growth became extensive only at *syn*- and post-eruptive conditions during lava flow. This observation has important implications for modelling the evolution of the viscosity of the lavas during their path on the surface.

The 1651–1654 eruption – object of this study - began in January 1651 CE with the opening of a WNW-ESE striking eruptive fissure located at 1800–1870 m a.s.l. on the western flank of Mount Etna and lasted until December 1654 CE. The lava flowed westward, destroying the neighbourhood of San Silvestro, damaging farmhouses and cultivated areas, and partially invading the town of Bronte (Branca and Abate, 2019), nowadays located at an elevation of 700–900 m a.s.l. The final composite lava field reached the elevation of 630 m a.s.l., extending ~10 km in length and covering an area of ~33 km^2. Nowadays, the 1651–1654 lavas are bordered and partially overlapped in the north by the effusive products of the 1832 CE eruption and at the south by those of 1843 CE eruption (Fig. 1).

The lava field is made of the superposition of numerous lava flows having thickness up to 5 m and displaying characteristic 'pahoehoe' morphology (Fig. 2), given by smooth and ropy crust indicative of high fluidity compared to the more viscous 'aa' morphologies, more common at Mount Etna. It is worth to note that the formation of aa or pahoehoe crusts does not depend only on viscosity, but some other factors play a crucial role, among which the increase in the terrain slope is the most effective, imposing transition from pahoehoe to aa morphology.

The lavas of the 1651–1654 eruption are also characterized by the presence of pressure ridges, originating from the concomitant flowing and cooling processes in active flows (Walker, 1991; Anderson et al., 2012; Gregg, 2017). To investigate their solidification history, samples representative of the inner and outer portions of a single flow unit were collected and studied. Sampling was carried out collecting lava specimens from the vertical section of a 4 m high fractured pressure-ridge displaying typical slabby pahoehoe morphology (Harris et al., 2017) (Fig. 2a and d) and located ~2.5 km SE from the town of Bronte, at an elevation of ~940 m a.s.l. and a distance from the effusive fissure of 9 km (Fig. 1). The choice of this location was made considering its representativeness in terms of height, comparable with the average thickness of the flows composing the lava field, and its accessibility that allowed an easy sampling of the different portions. The investigated section is composed by a massive internal part (~3 m), overlapped by a vesicular one (~0.5 m), and topped by a ropy crust (0.5 m). A sampling step of 0.5–1 m from bottom to top of the single section was determined based on macroscopic evidence such as massive (BRO1 and BRO2 samples), vesicle-rich (BRO3 sample) or ropy (BRO4 sample) aspect of the flow (Figs. 2b, c, d).

3. Methods

3.1. Whole rock composition and mineral abundance

Whole-rock major and selected trace element abundances were determined on powder pellets with a Rigaku Supermini 200 benchtop sequential wavelength-dispersive X-ray fluorescence spectrometer (XRF). The uncertainty is less than 5 % on the determination of the major and minor element abundances based on the values of several USGS rock references. Loss on ignition (LOI) was measured by the gravimetric method, after roasting ~1 g of pulverized sample at 900 °C

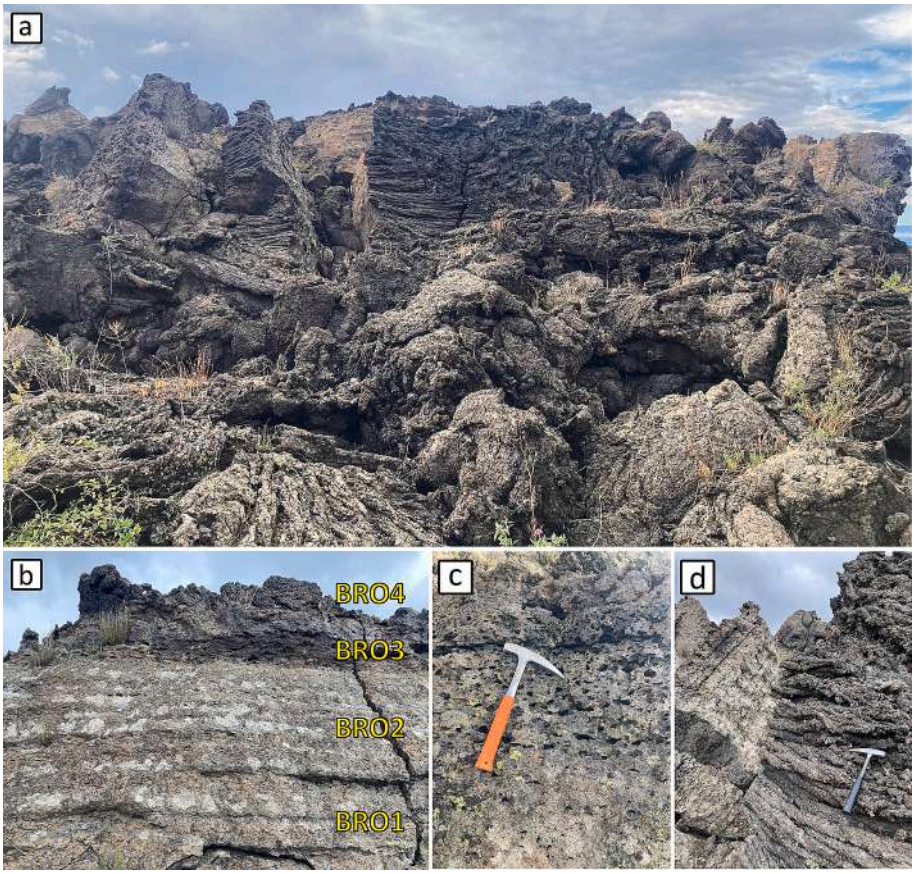

Fig. 2. Field pictures of the investigated lavas. a) general view of the investigated pressure ridge; b) sampled section inside the fractured pressure ridge, with the approximate location of the specimens along a vertical profile; c) detail of the BRO3 bubble rich layer, showing abundant centimetre-sized vesicles; d) typical ropy morphology of the lava crust (BRO4 sample).

for 24 h.

Mineral abundance by X-ray diffraction (XRD) measurements was determined by a Miniflex Rigaku X-ray powder diffractometer equipped with Ni-filtered Cu Kα radiation generated at 40 kV and 15 mA. The measurement was set at a scanning speed of 5.0°/min, steps of 0.0200° within the range of 5° to 65° (error ± 0.02°), for a duration of 14 min per sample. Qualitative analysis was performed via the search/match technique using the Profex 5.0.0 Software, while quantitative analysis of crystalline and amorphous phases was carried out using the Rietveld method and corundum as an internal standard (Gualtieri and Zanni, 1998).

3.2. Textural investigation

The textural investigation aimed to quantify the crystal and vesicle abundance in the four samples and was performed on two-dimensional (2D) images collected by SEM and on three-dimensional (3D) images acquired by X-Ray computed tomography. The 2D analysis allowed the quantification of the mineral (phenocrysts) abundances, whereas 3D images were used to retrieve information on the sole vesicle population. In fact, an accurate and reliable separation of the mineral phases (in particular plagioclase = plg, clinopyroxene = cpx and olivine = ol) on 3D images is prevented by the overlap of their greyscale colours (especially between cpx and ol) and by their fine and interconnected texture (especially among plg).

Textural investigations on SEM images were carried out by collecting and stitching tens of high-contrast back-scattered electron (BSE) images per sample with a Tescan Vega-LMU SEM at the University of Catania. Operating conditions were set at 20 kV accelerating voltage and ca 8 nA beam current for obtaining high-resolution BSE images. This allowed obtaining high-definition images of each thin section, useful for detailed analysis of the texture and for determining phenocryst abundances.

In order to characterize the vesicle population of the samples in three dimensions, high-resolution synchrotron radiation computed microtomography (SR μCT) measurements in phase-contrast mode (Cloetens et al., 1997) were carried out at the SYRMEP beamline of the Elettra – Sincrotrone Trieste laboratory in Basovizza (Trieste, Italy). Samples were prepared by cutting the original rocks into parallelepiped-shaped blocks with a size of about 4 mm × 4 mm × 8 mm. A polychromatic X-ray beam delivered by a bending magnet source illuminated the sample in transmission geometry. Filters (1.5 mm Si + 1 mm Al) were used to suppress the contribution of low energies in the beam spectrum, thus reducing the beam hardening effect. For each sample, a set of 1800 projections was recorded with an exposure time/projection of 125 ms. The detector used was an air-cooled, 16 bit, sCMOS microscope camera (Hamamatsu C11440—22C) with a 2048 × 2048 pixel chip coupled to a 17-μm-thick LSO scintillator screen. The effective pixel size of the detector was set to 1 × 1 μm, yielding a maximum field of view of ~2.4 mm × 2.4 mm. Scans were acquired in local or region-of-interest mode, working in phase-contrast mode, setting the sample-to-detector distance to 150 mm. This led to an increase in the visibility of the different phases present in the samples, thanks to an edge-enhancement effect at their borders (Cloetens et al., 1997).

Reconstruction of the 3D tomographic images was done with the Syrmep Tomo Project (STP) software suite (Brun et al., 2017), applying a single-distance phase-retrieval algorithm based on the transport of intensity equation of Paganin et al. (2002) to the acquired sample projection images before the reconstruction. Combining the use of phase-retrieval with the filtered back-projection tomographic reconstruction algorithm (Herman, 1980), the 3D distribution of the refraction index in the basaltic rocks was obtained. After manual optimization, the value of 50 for the $\delta/\beta = \gamma$ parameter (ratio between the real and imaginary parts of the complex refractive index) was chosen to enhance the contrast between the different crystalline phases within the rocks, keeping the blurring effects of phase-retrieval processing as low as possible.

Following the protocol reported in Lanzafame et al. (2020, 2022), representative volumes of interest (VOIs) were extracted from the original stacks of slices and segmented to isolate the sole vesicle phase. The determination of the abundance in vol% and of the morphological descriptors (size, aspect ratio, and sphericity) of the vesicles was obtained by the PyPore3D software library (Aboulhassan et al., 2022).

3.3. Mineral chemistry and element distribution maps

The major element composition of mineral phases was determined by electron probe micro analysis (EPMA) using a Cameca SXFive FE electron microprobe at the EPMA laboratory of the Core Facility Electron Beam Microanalysis, Faculty of Earth Sciences, Geography and Astronomy at the University of Vienna (Austria). The instrument is equipped with five wavelength-dispersive (WD) and one energy-dispersive (ED) spectrometers. Routine point analyses of olivine, oxides and clinopyroxene were performed using the following operating conditions: 15 kV accelerating voltage, 20 nA beam current, 20 s counting time on peak position, 1 μm beam diameter. For feldspar and glass, the beam was defocused to 5 μm and a 10 s counting time on the peak position for Na and K were used. Detection limits were: 100–250 ppm for Al, Na, Cr, Mn, Ti and Cl; 300–500 ppm for Si, Fe, Mg, Ca, Ni and K. Relative errors depend on the concentration of the elements in the unknown, being generally in the range of 1–2 % (1 sigma) for Si, Al, Fe, Mg and Ca in pyroxene, olivine, spinel, feldspar and glass. Relative errors for Ti and Cr in spinel and pyroxene are in the range of 1–5 % (1 sigma). Relative errors for Na and K in feldspar and glass are in the range of 1–5 % (1 sigma). Relative errors for minor elements such as Cr, Mn and Ni in olivine are in the range of 4–17 % (1 sigma; see also Casetta et al., 2025). For all analyses, natural and synthetic standards were used for calibration, and the PAP routine was applied for matrix correction (Pouchou and Pichoir, 1991).

Element distribution maps at the interface between plagioclase microlites and glass (see section 5) were acquired in beam scan mode using the same Cameca SXFive FE EPMA, with a 35.5 nA beam current and 10–15 kV accelerating voltage. Map size varied depending on the investigated microstructure, while a fixed step size of 0.33 μm and a dwell time per pixel of 40–80 ms were applied. Relative Fe, K, Mg, Na and Ti concentrations were mapped using five wavelength dispersive spectrometers set to the corresponding Kα emission wavelengths for each element, while Si, Al and Ca concentrations, being more abundant in both the glass and the plagioclase, were acquired through EDS.

3.4. Fourier Transform Infra-Red (FTIR) spectroscopy

Hydroxyl abundance in the groundmass glass of sample BRO4, representative of the outer portion of the lava flow, was quantified on doubly-polished thin sections using a Bruker Tensor 27 Fourier transform infra-red (FTIR) spectrometer located at the Department of Mineralogy and Crystallography of the University of Vienna. A globar was used as light source and a KBr beam as beam splitter. Measurement positions were identified on a Bruker Hyperion 1000 FTIR Microscope with a Cassegrain condenser and objective (×15, 0.4 nA) and a LN2 cooled MCT detector. Background and sample spectra were averaged from 128 scans in Bruker Opus 5.5.

Analyses were performed on a square 30 × 30 μm aperture, after ensuring by SEM and EPMA imaging the absence of gas bubbles, cracks and microlites. Water concentration was calculated according to Beer Lambert's law, considering that IR absorbances are directly related to the concentration of O—H units (whether OH or H_2O molecules) and the thickness of the sample as expressed by the equation:

$$A = \varepsilon \times c \times t \quad (1)$$

where $\boldsymbol{A}$ ($A = \log I_0/I$) is the measured IR absorbance of the peak at 3540 cm^{-1}, $\boldsymbol{\varepsilon}$ is the molar absorption coefficient, $\boldsymbol{c}$ is the concentration of O—H units in the unknown sample, and $\boldsymbol{t}$ is the sample thickness.

The analytic H_2O (including both OH and H_2O molecules) concentration (C_{H2O}) values (in wt%) were calculated from both linear and integrated absorbances (see Beran and Libowitzky, 2006; Libowitzky and Beran, 2006; Rossman, 2006). In the first case, C_{H2O} was calculated as:

$$C_{H2O}(wt.\%) = (\alpha \times 1.8)/(\varepsilon \times \rho) \quad (2)$$

Here, ε is the linear molar absorption coefficient (in $L \bullet mol_{H2O}^{-1} \bullet cm^{-1}$), ρ is the density of the glass (in $g \bullet cm^{-3}$), and α is the linear absorption coefficient (in cm^{-1}). The latter is obtained by dividing the linear absorbance A by the optical path length (i.e. sample thickness):

$$\alpha = A/t \quad (3)$$

In the case of the integrated absorbance, C_{H2O} was calculated as:

$$C_{H2O}(wt\%) = \left(\alpha_{i,tot} \times 1.8\right)/\left(\varepsilon_{i,tot} \times \rho\right) \quad (4)$$

Here, $\varepsilon_{i,tot}$ is the total integral molar absorption coefficient (in $L \bullet mol_{H2O}^{-1} \bullet cm^{-2}$), ρ is the density of the glass (in $g \bullet cm^{-3}$), and $\alpha_{i,tot}$ is the total integral absorption coefficient (in cm^{-2}). The latter is obtained by dividing the total integrated absorbance $A_{i,tot}$ ($A_{i,tot} = 3 \bullet A_i \pm 10$–20 % rel., Libowitzky and Rossman, 1997) by the sample thickness:

$$\alpha_{i,tot} = A_{i,tot}/t \quad (5)$$

The thickness of the studied sample, as measured by digital micrometer, was 120 ± 2 μm, and a density of the glass of 2.67 $g \bullet cm^{-3}$ was assumed after computation with the DensityX software (Iacovino and Till, 2019). The linear absorption coefficient ε was set at 75 $L \bullet mol_{H2O}^{-1} \bullet cm^{-1}$ according to Beran and Koeberl (1997), while the total integrated absorption coefficient $\varepsilon_{i,tot}$ was set at 79652 $L \bullet mol_{H2O}^{-1} \bullet cm^{-2}$ according to Libowitzky and Rossman (1997). As the characteristic bending vibration of H_2O molecules at ~1650 cm^{-1} is missing, the O—H stretching region at ca. 3200–3600 cm^{-1} must be assigned predominantly to OH groups. Nevertheless, because of the generally low hydrogen content, a minor non-detectable amount of molecular water cannot be excluded. All details and results are reported in Table 4.

4. Results

4.1. Whole rock analyses

On the Total Alkali Vs. Silica Diagram (Le Maitre et al., 2002), all the studied samples fall in the trachybasalt field, with average anhydrous composition of SiO_2 = 49.6 wt%, MgO = 4.25 wt%, $Na_2O + K_2O$ = 5.9 wt% (Table 1). This composition overlaps that of Recent Mongibello products in general, being in agreement with that of the plagioclase-rich lavas emitted in the 17th century of Mount Etna and matches with previous studies of the 1651–1654 lavas (Tanguy et al., 1997; Ferlito and Lanzafame, 2010; Nicotra and Viccaro, 2012; Lanzafame et al., 2013, 2022). All samples show homogeneity in the analysed trace elements content, with the exception of Cr and Pb that are sensibly higher than the average in BRO3 and BRO1, respectively (Table 1).

4.2. Texture and mineral chemistry

All the studied samples present the typical porphyritic texture of 'cicirara' lavas (Lanzafame et al., 2013), characterized by larger euhedral to subhedral phenocrysts of Plg and Cpx followed smaller by Ol and Ti—Fe oxides, with very scarce presence of small accessory minerals such as apatite. In the following descriptions, phenocrysts, microphenocrysts and microlites are identified based on the longest size dimensions >0.5, 0.5–0.3, and < 0.3 mm, respectively. The puzzles obtained by stitching BSE images collected by SEM (Figs. 1–4 in S1) cover an area of ~200 - ~450 mm^2 (Table 2) and highlight the textural variability from the massive inner portion (BRO1) to the vesicle-rich outer portion (BRO3) and the crust with pahoehoe structure (BRO4) of the lava flow (Fig. 2). All the samples present the same paragenesis, with slight differences in the crystal amount, given by phenocrysts of Plg (29.09–32.79 vol%), Ol (1.62–3.03 vol%) and Cpx (7.95–14.76 vol%), and Ti—Fe oxides (0.29–0.66 vol%) and a variable vesicle content, as high as 12.64 vol% in sample BRO3 (see Fig. 3 in S1 and Table 2). Nevertheless, the most striking textural difference among the samples can be observed in the groundmass features. Phenocrysts and microphenocrysts in samples BRO1, BRO2, and BRO3 are dispersed in a groundmass constituted by subhedral to anhedral microlites of Plg, Cpx, Ol and Ti—Fe oxides with sizes ranging from 0.3 mm to few μm and subordinate interstitial glass (Fig. 3). Conversely, sample BRO4 representative of the ropy crust has a groundmass which is dominated by the presence of glass (~60 area%), in which only few microphenocrysts and microlites of Plg and subordinate Cpx and Ol are recognized (Fig. 3).

Table 1
Whole-rock major and trace element compositions.

Sample	BRO1	BRO2	BRO3	BRO4	Average*
SiO_2	48.89	49.23	49.04	48.68	49.63
TiO_2	1.44	1.49	1.44	1.49	1.48
Al_2O_3	19.45	18.83	19.36	19.20	19.47
FeO	8.72	8.93	8.68	9.10	8.98
MnO	0.17	0.17	0.17	0.17	0.17
MgO	4.10	4.19	4.23	4.26	4.25
CaO	9.90	9.76	9.91	10.15	10.07
Na_2O	4.02	3.99	3.88	3.72	3.95
K_2O	1.52	1.55	1.50	1.47	1.53
P_2O_5	0.47	0.49	0.46	0.41	0.46
Tot	98.67	98.65	98.67	98.63	100.00
Sr	1181	1096	1144	1190	1153
V	234	231	222	210	224
Cr	34	30	53	35	38
Ni	33	25	33	28	30
Rb	32	33	31	35	33
Y	27	24	23	25	25
Zr	210	216	209	215	213
Nb	42	47	45	46	45
Ba	1795	1870	1850	1720	1809
Pb	26	14	17	18	19

* Normalized average values.

Plg is the most abundant phase in all samples (Table 2), with phenocrysts having sizes of up to 6 mm and displaying complex grain internal textures (Fig. 4) characterized by inclusion-free and homogeneous areas together with sieve texture and patchy zoning (Giacomoni et al., 2014). Smaller individuals (< 1 mm) are often homogeneous, whereas larger ones (> 1 mm) display either inclusion/texture-free cores surrounded by sieved and patchy mantle or sieved and patchy cores surrounded by inclusion/texture-free mantle (Fig. 4). Large individuals frequently show oscillatory zoning with compositional fluctuations extending over a few tens of μm in radial direction, together with dusty concentric portions containing numerous inclusions of Ti—Fe oxide crystals (Fig. 4). Results of compositional core-to-rim profiles and of single-spot analysis on groundmass microlites are reported in the supplementary material (Table 1 in S2 and Figs. 5 and 6 in S1). The phenocrysts generally display Ca-rich cores ($An_{77–55}$) compared to rims ($An_{69–36}$). However, the transition from An-rich cores to Ab-rich rims is not continuous: the core-to-rim profiles (An_{70} to An_{54} on average, see Fig. 5 in S1 and Table 1 in S2) are characterized by large scale compositional oscillations (hundreds of μm), corresponding to sieve or dusty textured areas (Fig. 4). These latter display a general enrichment in the An content (Fig. 5 in S1). Rims of phenocrysts are mostly well defined and neat, with no textural evidence of resorption or disequilibrium during or after their growth. Microlites of Plg display an ample compositional range, broadly similar to that of Plg rims ($An_{66–39}$) and are abundant in the BRO1, BRO2 and BRO3 samples, where they constitute a large part of the groundmass, being instead rare in the glassy

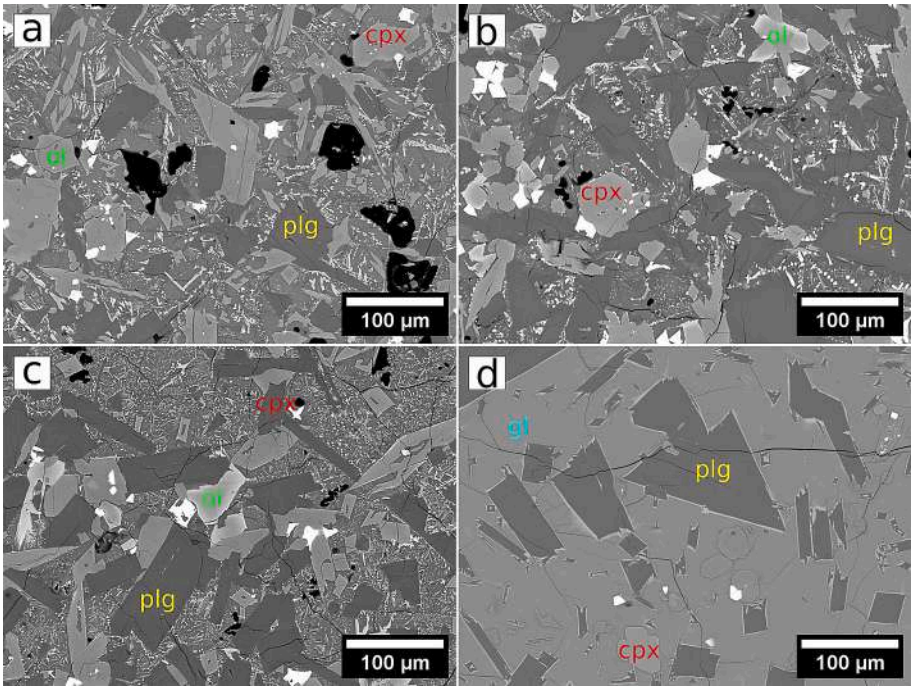

Fig. 3. Texture of the groundmass in samples a) BRO1, b) BRO2, c) BRO3 and d) BRO4. The BSE images display a texture difference, with an evident increase in the glass abundance from a) to d).

groundmass of sample BRO4. In this sample, grains of the smallest population of Plg microlites have skeletal texture and are surrounded by thin (1–2 µn) chemical boundary layers, white-coloured in BSE images, at the interface with the surrounding glass (Fig. 3). The significance of these chemical boundary layers is discussed in the next sections.

Cpx is the second most abundant phase, with phenocrysts reaching a size of 6 mm and often presenting euhedral to subhedral habitus, whereas microlites in the groundmass are mostly anhedral (Fig. 4). All analysed crystals have diopsidic or augitic composition, with no evident differences among the four samples (Table 2 in S2 and Fig. 7 in S1). The average compositions of the diopsidic phenocryst cores (Mg# 75, $DiHd_{81}$) are slightly enriched in Mg compared to the rims and the groundmass grains (Mg# 71, $DiHd_{78–79}$).

Ol phenocrysts are volumetrically subordinate to Cpx and appear as a few subhedral and < 1 mm-sized individuals (Fig. 4). In rare exceptions (1–2 crystals per sample), they reach sizes of 3 mm. In all samples, Ol phenocrysts show a narrow compositional range, with average values of $Fo_{73–75}$ in the cores and $Fo_{71–72}$ in the rims. However, some crystals display higher Mg contents in the cores (up to Fo_{82}) or, conversely, Fe rich rims (Fo_{67}) (Table 3 in S2 and Fig. 8 in S1). Groundmass microlites are always subhedral to anhedral and have a wider average composition ($Fo_{67–71}$), with some individuals showing high Fe content (Fo_{53}).

4.3. Glass amount and composition

The samples from the inner portion of the investigated flow (BRO1 and BRO2) and the vesicle-rich zone (BRO3) contain glass only as interstitial phase between the microlites, whereas the sample from the ropy crust of the flow (BRO4) has a glass-dominated groundmass. Although recognizable by SEM and SR µCT, quantification of glass by image analysis is prevented by its greyscale tone, often overlapping with that of the microlites. The quantification was therefore determined by XRD analysis, revealing values progressively increasing from 21.7 wt% in BRO1 to 48.3 wt% in BRO4 (Table 3 and Figs. S1-S4). Along with the increasing modal abundance, EPMA spot analyses reveal a progressive decrease in the SiO_2 and FeO/MgO ratio and a parallel increase in alkali content ($Na_2O + K_2O$) and CaO/Al_2O_3 ratio from BRO1 to BRO4, i.e., from the base to the top of the lava flow (Fig. 5; Table 4 in S2). According to FTIR measurements, the H_2O content of the groundmass glass at the top of the lava flow (ropy crust) ranges from 0.07 to 0.14 wt% (Table 4), confirming the almost complete loss of H_2O during post-eruptive degassing. On the other hand, these results highlight that small amounts of H_2O can be retained within the melt at post-eruptive conditions, with a potential effect on its degree of polymerization and ultimately on the crystallization dynamics.

4.4. Vesicle content and morphology

The vesicle content and morphology were measured both employing 2D and 3D techniques for large (mm-sized) and small (µm-sized) ones. It is worth noting that the different scale adopted in the two methodologies led to very different results in vesicle abundance. Indeed, image analysis of 2D puzzles allows to investigate large areas, adequate to include the mm-sized vesicles obtaining an accurate estimation of the vesicle abundance, but this approach does not allow to retrieve accurate information on the 3D morphology of the vesicles. Conversely, the small volumes investigated by SR-µCT are not representative of the large-scale variation of textural features along the vertical profile of the lava flow, but provide robust information on the morphology of the micrometric vesicles which are related to the *syn*-eruptive degassing of the lavas (Polacci and Papale, 1997; Lanzafame et al., 2022).

Results of the 2D investigations confirm the observation made at the macro-scale in the field: the inner and massive portion of the lava flow contains only 5–8 area% of voids with a number density of ~78–80 bubbles/mm^2, while the external portions of the flow are richer in vesicles, with the highest amount of 12.64 area% and 173 bubbles/mm^2 in BRO3, and a slightly lower content of 10.9 area% and 160 bubbles/mm^2 in the crust (Table 5).

At the micron scale, results of X-ray SR-µCT (Fig. 6) allowed for the characterization of the smallest bubbles with sizes in the range of 10–1000 µm. These vesicles occupy 3–5 vol% of the investigated volumes, are slightly deformed (see values of sphericity in Table 5), have an average volume of 10^{-5} - 10^{-6} mm^3, and a number density that varies between 10^4 and 10^3 bubbles/mm^3. The vesicle size distribution (Fig. 7)

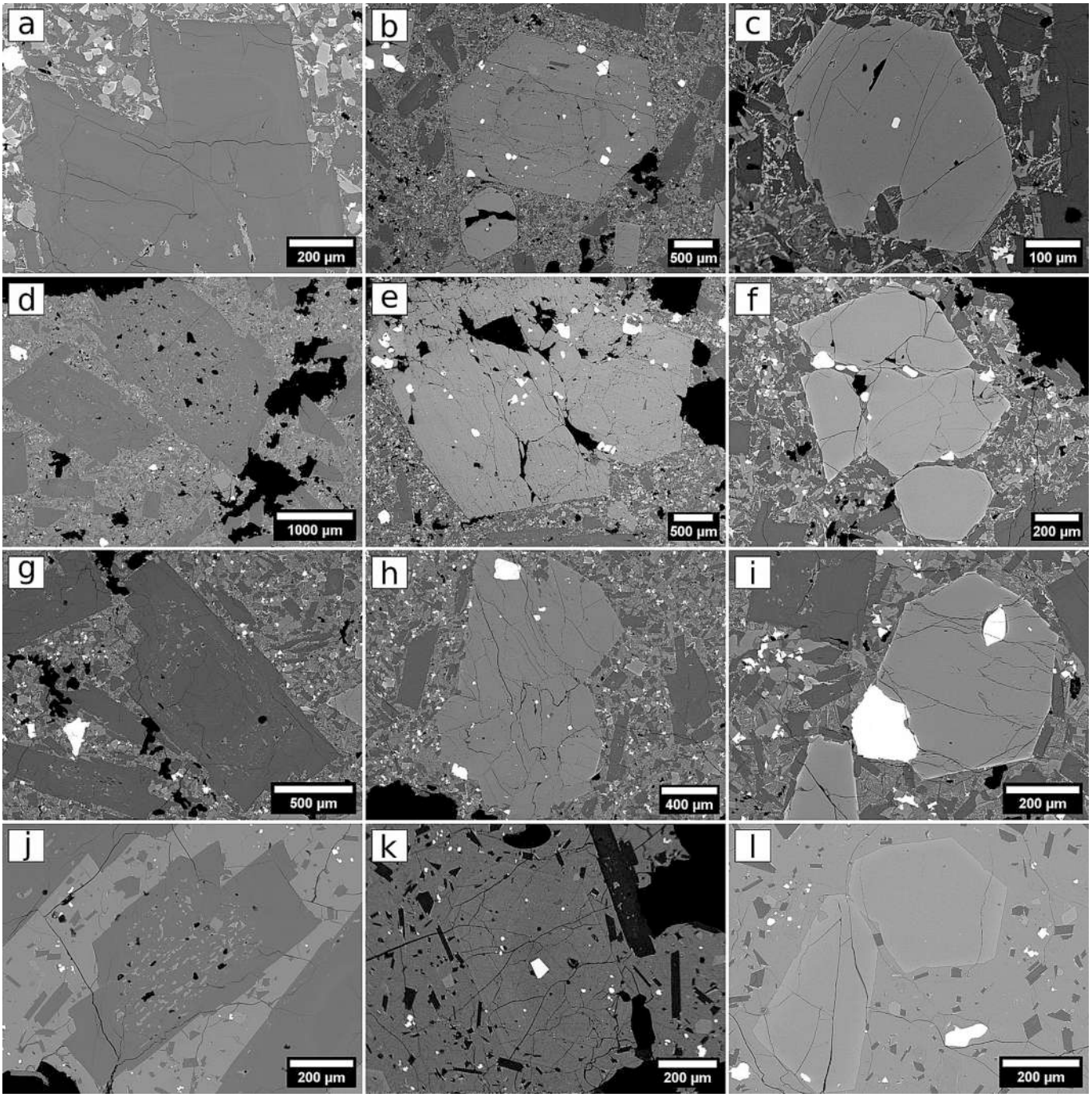

Fig. 4. Main textures of Plg (a, d, g, j), Cpx (b, e, h, k) and Ol (c, f, i, l) phenocrysts of the samples, displayed from top (BRO1) to bottom (BRO4). See the text for descriptions.

Table 2
Amount of phenocrysts, glass, groundmass and vesicles (area%) determined by 2D analysis of thin sections.

Sample	Investigated area (mm^2)	Plg*	Cpx*	Ol*	Timt*	Gm + Glass*	Vesicles
BRO1	329.28	32.79	7.95	2.93	0.52	55.81	5.39
BRO2	453.48	29.09	14.76	1.70	0.66	53.80	8.07
BRO3	334.23	31.22	12.25	3.03	0.29	53.21	12.64
BRO4	209.46	31.18	8.52	1.62	0.41	58.28	10.90

* Normalized to vesicle-free area; Plg = Plagioclase, Cpx = Clinopyroxene, Timt = Titanomagnetite, Gm = Groundmass.

depicts a clear trend from the inner to the outer portions of the flow. The number frequency diagram (Fig. 7a) indicates that all the distributions are unimodal and peaked at 10^{-7} mm^3. The fraction of the number of vesicles in this range increases from BRO1 to BRO4. The volume frequency distributions (Fig. 7b), however, indicate that these small vesicles contribute less than 5 % of the total porosity, which is instead

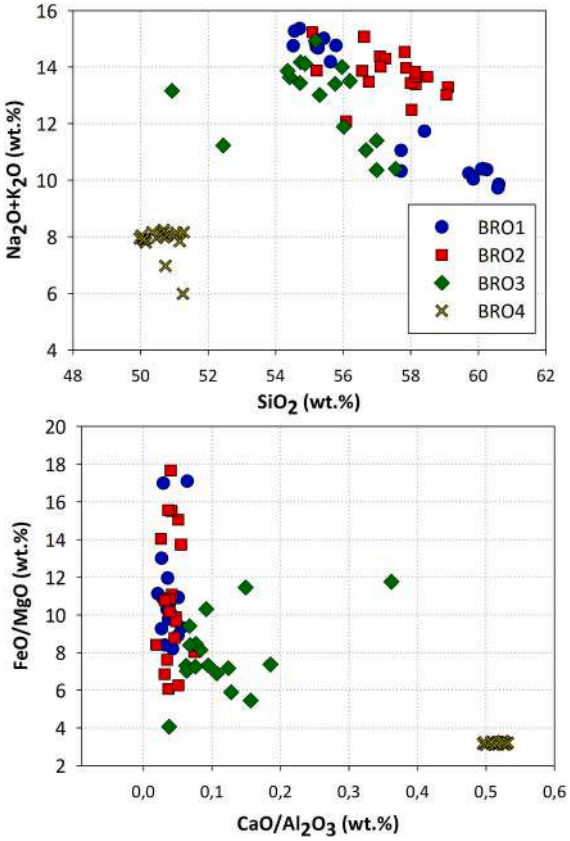

Fig. 5. Composition of glass in the four BRO samples, showing a progressive decrease of the average FeO/MgO ratio and SiO_2 and alkali content, and a parallel increase of the CaO/Al_2O_3 ratio from the inner (BRO1–2) to the outer (BRO3–4) samples.

Table 3
Results of quantitative XRD analysis.

Sample	Aug	Fo	Mag	Plg	Am
BRO1	19.90	5.26	2.21	50.93	21.70
BRO2	17.76	4.75	2.74	50.55	24.20
BRO3	16.60	3.74	1.16	47.01	31.50
BRO4	11.61	3.41	1.11	35.58	48.30

Aug = Augite; Fo = Fosterite; Mg = magnetite; Plg = Plagioclase; Am = Amorphous phase.

mainly given by a few vesicles with sizes in the range of 10^{-2} mm^3.

5. Discussion

5.1. Pre-eruptive crystallization and crystal cargo of the lava flow

The crystallization history and the pre-eruptive pressure (P) and temperature (T) conditions of the magma feeding the 1651–1654 eruption were modelled using thermobarometric equations based on crystal-melt equilibrium and considering the progressive evolution of the melt composition due to crystal fractionation. As the high crystal cargo of the lavas prevents the use of their bulk-rock composition as a representative of a liquid (with the exception of the first nucleating phase), mineral-melt pairs were therefore established starting from the bulk-rock composition (M1 in Table 6) and progressively subtracting by mass balance the composition of the minerals appearing on the liquid line of descent, following the equation:

$$X_{liq} = \frac{X_{wr} - (X_{xls_1} \times \Phi_{xls_1}) - \bullet\bullet\bullet - (X_{xls_n} \times \Phi_{xls_n})}{1 - (\Phi_{xls_1} + \bullet\bullet\bullet + \Phi_{xls_n})} \quad (6)$$

where X_{liq} is the chemical component in the intermediate liquid expressed as oxide wt%, X_{wr} is the whole-rock composition, X_{xls} is the concentration of the component in the minerals as obtained by EPMA analyses and Φ_{xls} is the weight fraction of the mineral phase retrieved by petrographic analysis. This procedure is necessary to reconstruct the composition of the melts on the liquid line of descent and to couple it with the equilibrium mineral phase before thermo-barometric estimates.

The liquid-line of descent of Mount Etna parental magmas have been depicted by petrographic evidences, experimental petrology (Métrich and Rutherford, 1998; Mollo et al., 2015a, 2015b) and thermodynamic simulations (Trigila et al., 1990; Armienti et al., 1988, 2012; Corsaro and Pompilio, 2004a, 2004b; Giacomoni et al., 2014; Kahl et al., 2014)

Table 5
Results of vescicles analysis of 3D images from SR μCT experiments.

	VOI (voxel)	VOI (mm^3)	Number Density (mm-3)	Amount (vol%)	Volume* (mm^3)	Sphericity*
BRO1	1200 × 1461 × 1792	3.14	10,053	4.82	4.79E-06	0.76
BRO2	1329 × 1461 × 2841	5.52	4707	3.18	6.75E-06	0.76
BRO3	1259 × 1521 × 5372	10.29	2833	5.01	1.81E-05	0.75
BRO4	1203 × 1569 × 3239	6.11	1371	3.23	2.36E-05	0.76

* Average values.

Table 4
Parameters adopted to calculate H_2O concentrations (wt%) from FTIR absorption measurements on glasses in sample BRO4. A density of 2.67 g/cm^3 for the glass was considered according to Iacovino and Till (2019).

Sample	Thickness#	Integrated Absorbance*	Integrated Abs.-Coeff.	Molar Abs.-Coeff.+	H_2O+	Linear Absorbance	Linear Abs. Coeff.	Molar Abs.-Coeff.§	H_2O§
spot	[μm] (±2)	[cm^{-1}] (±2)	[cm^{-2}]	[cm^{-2} per mol H_2O/L]	[wt-%]		[cm^{-1}]	[cm^{-1} per mol H_2O/L]	[wt-%]
BRO4_gl4	120	66.20	5517	79,652	0.140	0.12	10.00	75	0.090
BRO4_gl5	120	59.70	4975	79,652	0.126	0.11	9.17	75	0.082
BRO4_gl6	120	50.90	4242	79,652	0.108	0.09	7.50	75	0.067

Thickness from digital micrometer.
* Range of integration: 3750–2830 cm^{-1}, mean wavenumber: 3430 cm^{-1}.
+ Libowitzky and Rossman (1997), "General, wavenumber-dependent IR calibration", $A_{i,tot} = 3 * A_i$, ± 10–20 rel-%.
§ Beran and Koeberl (1997), ± 5 rel-%.

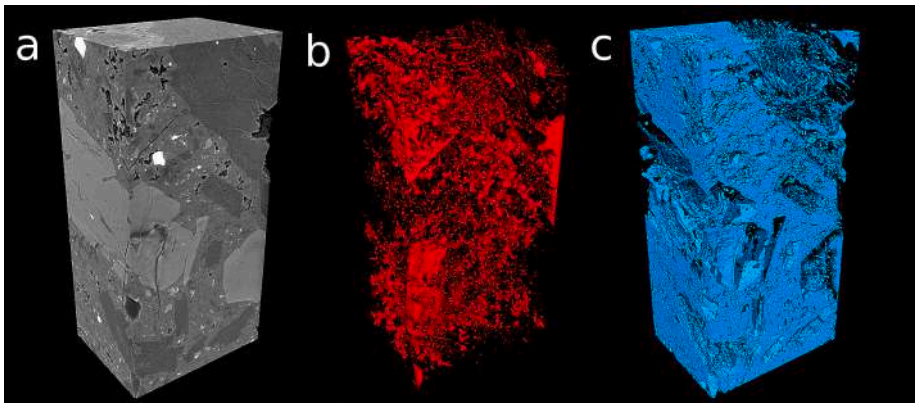

Fig. 6. 3D renderings of the analysed *V*olume of Interest (VOIs) from BRO4 sample (6.11 mm^3). a) reconstructed VOI in greyscale: dark tones = vesicles, dark grey = Plg, grey = glass, light grey = mafic phases (Cpx and Ol), bright tones = titanomagnetite; b) 3D rendering of the segmented vesicle phase; c) 3D rendering of the segmented glass phase.

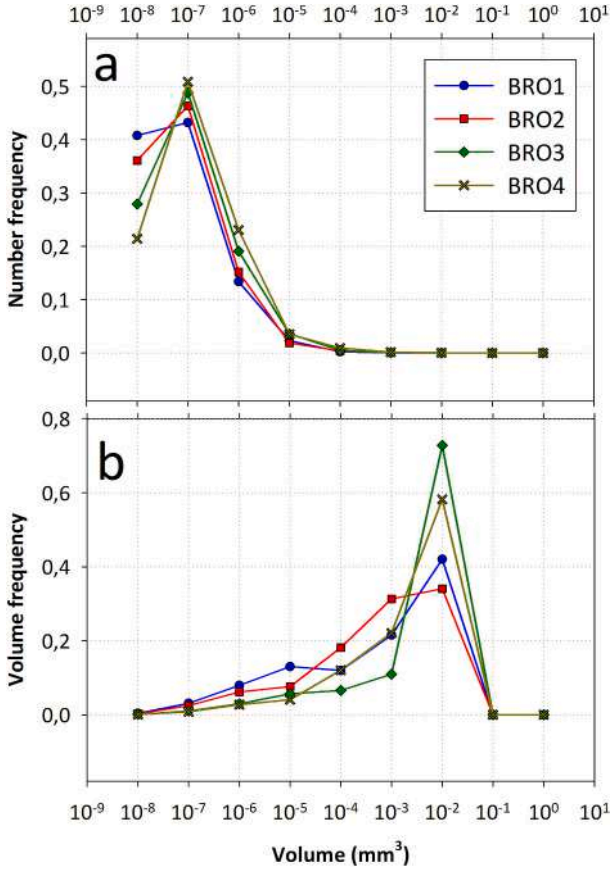

Fig. 7. Results of the vesicle morphology analysis: a) vesicle number frequency computed as the fraction of number of vesicles having a given size range over the cumulative number of vesicles; b) vesicle volume frequency calculated as fraction of volume of vesicles having a given size range over the cumulative volume of vesicles.

that evidenced that Ol is commonly the first phase on the liquidus in less evolved magmas. However, since most of historic erupted lava differentiate up to 15 % Ol en-route to the surface (Kahl et al., 2014; Giacomoni et al., 2014 and references therein), they are typified as Ol and Cpx appearance as cotectic phases. On these bases, the reconstruction of 2 equilibrium melts (M2 and M3 in Table 6) relies on the following assumptions:

Table 6
Results of mass balance calculations using eq. (6) and (7). All compositions are expressed in normalized oxide wt%.

Melt label	M1	M2	M3	M4
Equilibrium with	Ol core	Cpx core	Plg core	Ol-Cpx-Plg rim, gm
Composition	WR	WR - 2.5 % Ol	Gl + 30 % Plg	Gl
SiO_2	49.63	50.16	51.21	50.27
TiO_2	1.48	1.46	1.51	2.40
Al_2O_3	19.47	20.04	20.68	15.35
FeO	8.98	8.30	7.27	11.41
MnO	0.17	0.17	0.00	0.00
MgO	4.25	3.37	2.24	3.58
CaO	10.07	10.37	9.88	8.08
Na_2O	3.95	4.08	4.48	4.72
K_2O	1.53	1.58	2.07	3.12
P_2O_5	0.47	0.48	0.66	1.08

WR = average whole rock composition of samples from XRF analysis; Ol = olivine; Cpx = clinopyroxene, Plg = plagioclase; Gl = glass.

- high-$Fo_{(88–80)}$ Ol is the first phase on the liquidus, in equilibrium with M1;
- high-Mg# Cpx and Ol $Fo_{(80–70)}$ are cotectic, in equilibrium with M2;
- Fe—Ti Oxides appear along the whole liquid line of descent;
- Plg crystallizes as the last phase, in equilibrium with M3;
- the growth of each nucleated individual continues throughout the entire magma migration;
- microlites in groundmass crystallized from a liquid with BRO4 glass composition (M4).

The composition of the reconstructed melts is reported in Table 6. The initial H_2O content in the melt was set to a conservative value of 4 wt%, according to the recent advances in the study of melt inclusions indicating that primary Etnean alkaline magmas can contain up to 6 wt % of dissolved H_2O (Gennaro et al., 2019; Giacomoni et al., 2021, 2024).

The crystallization T of Ol cores (T_{ol}) was determined using eq. 22 of Putirka (2008) on crystal-melt (M1) pairs in the range of equilibrium defined by the $^{ol\text{-}liq}Kd_{Fe\text{-}Mg} = 0.3 \pm 0.03$ (Fig. 8a) and setting $P = 7$ kbar, the lowest P at which $T_{ol} \geq T_{cpx}$, and fO_2 = QFM + 1 (D'Orazio et al., 1998; Mollo et al., 2011; Giacomoni et al., 2014). Results indicate that Ol cores ($Fo_{73–76}$) formed at an average T of 1070 ± 29 °C.

The P-T crystallization conditions of Cpx cores from M2 (Table 6) were determined through mineral−melt exchange reactions of Di/Hd-Jd and Hd/Ca-Tsch Putirka (2008), considering only cores that attained the equilibrium condition within the range of $^{cpx\text{-}liq}Kd_{Fe\text{-}Mg} = 0.27 \pm 0.03$ (Fig. 8b, Putirka et al., 2003; Mollo et al., 2015a, 2017). Most of the

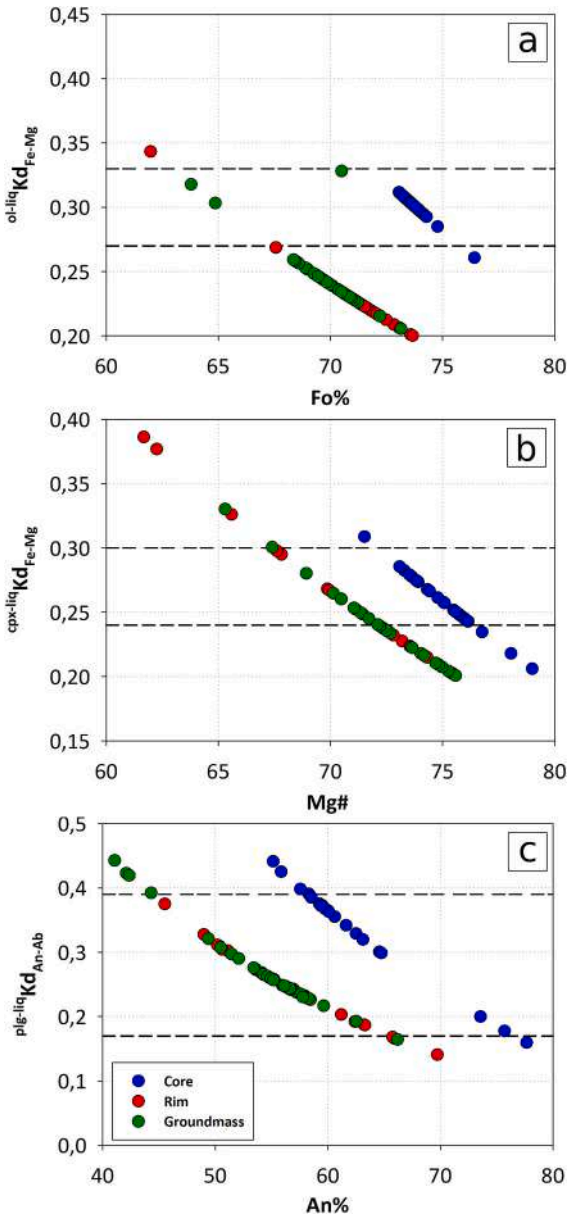

Fig. 8. Results of partition coefficient determination for Ol, Cpx and Plg and equilibrium ranges indicated by dotted lines within each diagram. a) Forsterite (Fo%) vs. $^{Ol\text{-}Liq}Kd_{Fe\text{-}Mg}$ diagram for Ol crystals, $^{Ol\text{-}Liq}Kd_{Fe\text{-}Mg} = 0.27–0.33$ from Roeder and Emslie (1970); b) Mg# vs. $^{Cpx\text{-}Liq}Kd_{Fe\text{-}Mg}$ diagram for Cpx crystals, $^{Cpx\text{-}Liq}Kd_{Fe\text{-}Mg} = 0.24–0.30$ from Mollo et al. (2015a) and Putirka et al. (2003); c) Anorthite (An%) vs. $^{Plg\text{-}Liq}Kd_{Ab\text{-}An}$ diagram for Plg crystals, $^{Plg\text{-}Liq}Kd_{Ab\text{-}An} = 0.17–0.39$ considering $T > 1050$ °C from Putirka (2008).

investigated Cpx cores are in equilibrium with a composition obtained by subtracting up to 2.5 % of Ol from the whole rock composition. T and P were estimated using eqs. 33 and 32b, respectively, in Putirka (2008), following the recent reliability assessments of Wieser et al. (2023a, 2023b). Results indicate that the phenocrysts cores formed at an average T of 1069 ± 25 °C in a large P range of 6.29–3.09 ± 1.7 kbar.

The conditions of the crystallization of the Plg cores were modelled assuming their crystallization from a slightly more evolved liquid (M3 in Table 6). Indeed, the crust of the lava flow (BRO4 sample) displays a great abundance of glass (~55 %) in which phenocrysts of Fe-rich Ol (Fo < 80), Fe-rich Cpx and Plg are dispersed. To retrieve the composition of the M3, mass balance calculations were performed by adding the Plg average composition (Table 6) to the glass taking into account that Plg and glass density have similar values:

$$X_{liq} = \frac{(X_{gl} \times \Phi_{gl}) + (X_{plg} \times \Phi_{plg})}{\Phi_{gl} + \Phi_{plg}} \quad (7)$$

where X_{liq} is the component expressed as oxide in wt%, $\Phi_{gl} = 0.55$ is the fraction of glass and $\Phi_{plg} = 0.30$ the fraction of Plg phenocrysts in the rock. The obtained melt composition M3 (Table 6) is intermediate between the composition of the whole rock and that of the glass.

Following Putirka (2008), the equilibrium between Plg cores and the M3, and between Plg rims/groundmass and glass (M4) was checked considering $^{plg\text{-}melt}Kd_{Ab\text{-}An} = 0.28 \pm 0.11$. Results (Fig. 8c) indicate that most of the Plg fall in the equilibrium with the reconstructed melts. The content of dissolved H_2O in the melt was obtained by applying the hygrometer of Waters and Lange (2015), which is based on exchange reactions between Ab and An components. The calculation was made on Plg cores, assuming $T = 1065$ °C and $P = 4$ kbar, accordingly with the lower estimates obtained from Ol and Cpx thermobarometry. Results indicate a H_2O content of 4.6 wt% (Fig. 9a) with an error of ±0.35 wt% at P = 4 kbar: this result is in agreement with degassing simulation (Fig. 9b) performed using the SolEx software (Witham et al., 2012) which indicates an exsolution threshold at $P < 2.5$ kbar for a trachybasalt containing 4 wt% H_2O. The application of the same hygrometer to Plg rims and microlites, assuming $T = 1060$ °C and $P = 1$ bar, yields a H_2O content of 0.9–1 wt%.

5.2. Syn-flow degassing

Along with triggering and driving eruptive mechanisms in the upper portion of volcanic feeding systems (La Spina et al., 2022; Bamber et al., 2024; Bonechi et al., 2024), vesicle nucleation, growth and coalescence in silicate melts strongly influence some of the crucial physical properties of lava flows, particularly viscosity. Experimental works demonstrated that vesicle abundance and shape can significantly influence the rheology of the lava: generally, it is assumed that an increasing vesicle content reduces viscosity, but the extent of this effect varies depending on whether the bubbles are spherical or deformed (Rust and Manga, 2002; Llewellin and Manga, 2005; Mader et al., 2013; Truby et al., 2015). Vesicles can originate from gas exsolution from the melt at pre-eruptive conditions and are passively dragged within the lava as it flows on the surface. Theoretical studies and thermo-hygrometric models on natural samples showed that H_2O exsolution in Mount Etna basaltic/trachybasaltic melts usually start to occur at around 2–2.5 kbar (Giacomoni et al., 2021) and continues along the ascent up to the surface. For the studied 1651–1654 CE eruption, simulations with the SolEx software (Witham et al., 2012) confirm this data, suggesting that a melt with initial H_2O content of ~4 wt% begins exsolving H_2O at $P < 2.5$ kbar (Fig. 9b).

Yet, a significant portion of vesicles can also be produced at post-eruptive conditions, due to the retention of residual volatiles, mostly H_2O, within the lava (Walker, 1991; Polacci and Papale, 1997; Harris et al., 2017). This leads to continuous vesicle nucleation, growth, and coalescence during lava flow and after emplacement (Lanzafame et al., 2022). In our case, 2D observations at the millimetre scale indicate a lower vesicle content in the inner portions of the lava flow (BRO1 and BRO2) compared to the outer sections (BRO3 and BRO4), suggesting active bottom-to-top vesicle migration during flow. Furthermore, 3D analyses at micron scale reveal a decrease in the number frequency of very small vesicles (10^{-8} mm^3) from BRO1 to BRO4 (Fig. 7a). This trend is likely due to the lower cooling rates at the inner portion of the flow, allowing prolonged degassing and the nucleation of a higher number of small vesicles compared to the rapidly solidified crust. The inversion in the number frequency distribution trend at 10^{-7} mm^3 (Fig. 7a) is due to vesicle coalescence towards the upper portions of the flow, a process further supported by volume frequency distribution data (Fig. 7b). Specifically, vesicles $>10^{-2}$ mm^3 constitute 58–72 % of the total vesicle volume in BRO4 and BRO3, respectively, versus the 42–34 % in BRO1

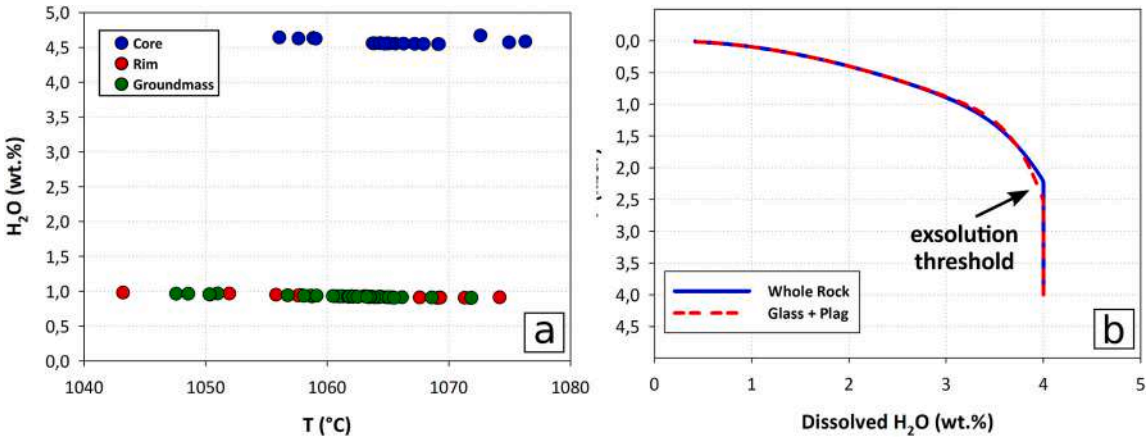

Fig. 9. Water content of the melt and degassing path of the magma; a) water content determined hygrometry on Plg crystals using the model of Waters and Lange (2015); b) Dissolved water in the melt as function of pressure modelled by SolEx software (Witham et al., 2015), assuming two compositions equal either to the whole rock (in equilibrium with Ol) or to the glass + dissolved Plg (in equilibrium with Plg cores); modelling of degassing was done considering an initial CO_2 = 4000 ppm, S = 2800 ppm and Cl = 1400 ppm according to melt inclusion in Ol from trachybasalts erupted at Mount Etna (Métrich et al., 2004; Spilliaert et al., 2006).

and BRO2. These trends suggest that the emplacement of the 1651–1654 lavas was accompanied by active degassing of a consistent residual volatile content in the melt during the flow.

The presence of volatiles in silicate melts, either dissolved or exsolved as vesicles, has important implications for the investigation and prediction of the behaviour of active lava flows, as it decreases viscosity with significant changes on the rheology of lavas and therefore on their path when flowing on the surface (Harris and Rowland, 2001; Herault et al., 2009; Kelfoun and Vargas, 2016; Chevrel et al., 2018; Lanzafame et al., 2022). EPMA analyses show that glasses in the inner portion of the lava flow retain 0.3–0.7 wt% Cl, while glasses in the pahoehoe crust have a lower and constant concentration of Cl (0.16–0.20 wt%; Table 4 in S2). This testifies to the active degassing of the lava during flowing, and/or the concomitant crystallization of mineral phases hosting Cl, such as apatite, in the microcryst assemblage. The FTIR measurements show that a low but not-negligible amount of H_2O (0.08–0.17 wt%) remained dissolved in the glassy groundmass of sample BRO4 (Table 4). It is worth to remark that this amount represents only the water content at the moment of final quenching of the crust of the flow, occurred after that the investigated lava experienced 9 km of flowing (see Fig. 1) and degassing at disequilibrium condition on the surface.

5.3. Syn- to post-eruptive solidification

To reconstruct the subaerial processes of crystallization, it is necessary to retrieve the proportions of crystals and melt already present at the moment of the eruption. Thus, it is required to discern the portion of the investigated lava flow that best represents the state of the magma suspension (crystal + melt + vesicles) as it was emitted on the surface. This can be done by considering the textures of the BRO4 sample, collected from the crust of the lava flow. In fact, the crust is the portion of the flow in direct contact with the cold air and therefore subjected to cooling rates orders of magnitude higher than the inner portions (Harris et al., 2005). At these conditions, lava quenches very rapidly, over time spans on the order of minutes, preserving the original texture of the silicate melt at the time of its emission.

The XRD data and image analysis of this sample indicate that moments after its discharge on the surface the lava comprised ~40–50 % of crystals, mostly phenocrysts, and ~ 50–60 % of melt. According to the $^{\text{mineral-melt}}Kd_{Fe\text{-}Mg}$ data, Ol and Cpx phenocrysts rims and microlites in sample BRO4 are in strong chemical disequilibrium with respect to the surrounding glass (Fig. 8a and b). Yet, their euhedral morphology suggests growth at close to equilibrium conditions (Fig. 4l). On the contrary, the rims of Plg phenocrysts and the core of the microlites are in chemical equilibrium with the surrounding glass (Fig. 8c). Hygro- thermometric models indicate that these crystals formed at T = 1060 °C from a melt with dissolved water content of ~1 wt% (Fig. 9), which most likely represents the initial condition of the subaerial flow of the 1651–1654 lavas. Interestingly, Plg microlites show skeletal morphology and the presence of a chemical boundary layer (CBL) at the contact between microlite and the surrounding glass, which is bright in BSE images (Figs. 10 and 11). Other authors documented the existence of Fe-rich CBLs at the Plg-melt interfaces in tephra products from Etna and Stromboli volcanoes (Pichavant et al., 2022; D'Oriano et al., 2025), and in the Kilauea Iki lava lake (Honour et al., 2019). These CBL domains form due to disequilibrium crystal growth taking place in very short time spans (seconds to minutes), and, if preserved as filaments within the melts, can bear witness of interaction between magmas with different temperature and volatile contents (D'Oriano et al., 2025).

The acquisition of high-resolution element maps by EPMA at low-voltage conditions shows that the core of Plg microlites is relatively Ca-rich compared to the outermost 1–5 μm wide rim, which is more albitic (Figs. 10 and 11). With respect to the unaffected glass far from the grains, the surrounding CBL is characterized by an enrichment in MgO, FeO, TiO_2, and CaO and a depletion of SiO_2 and Al_2O_3. Moreover, in most of these plagioclases, short tails (<1 μm) are present at all corners, beyond which no significant CBL is observed. From a theoretical point of view, a CBL can form when chemical components that are incompatible in a fast-growing crystal accumulate in the glass immediately in front of the crystallization front (Zhang et al., 2010; Zellmer et al., 2016). The extent of accumulation/depletion of a specific component depends on: i) the concentration difference of this component between the glass and the growing crystal, and ii) the competing effects of diffusion of the component in the melt and the delivery/extraction of the component to/from the melt at the crystallization front due to repulsion from/fractionation into the growing crystal (Levich, 1962). In our case, elements with low partition coefficient (K_D) with respect to Na-enriched Plg, like Mg, Fe, Ti and Ca, preferentially partition into the melt, while elements such as Si, Al and Na are more compatible in the Plg. The incompatible elements pile-up at the moving Plg-melt interface (crystallization front), and can be preserved as a CBL only if their diffusivities in the melt are too slow to effectively homogenize the component that is locally delivered to/removed from the melt at the crystallization front in the melt. The preservation of such features in lavas offers the unique opportunity to apply diffusion chronometry models to retrieve the rate of crystal growth of the Na-rich rim present in the Plg microlites in the crust of the pahoehoe lava.

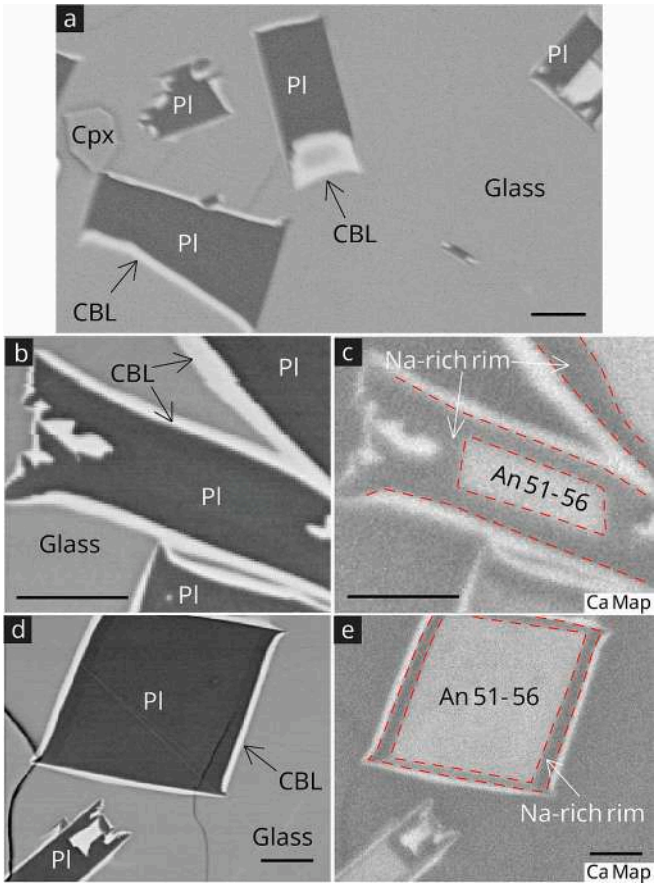

Fig. 10. a) BSE image of the groundmass of a Bronte lava near the contact with air. b-d) high magnification BSE image of Plg micro-crystals (dark grey) surrounded by CBLs (white). c-e) EPMA chemical map (scanned at 15 kV) showing Ca relative amount in the phases composing the scanned area. All scale bars are 10 μm long.

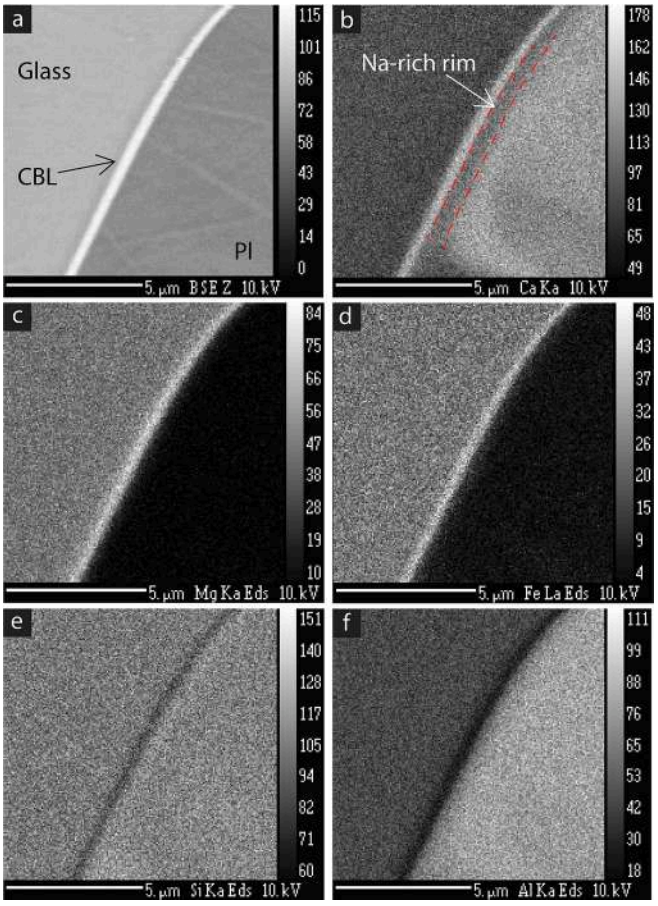

Fig. 11. a) BSE image of the Plg-CBL-melt system selected for a high-resolution EPMA scan (10 kV). b-f) Ca, Mg, Fe, Si and Al elemental EPMA maps of the same area of (a).

Compositional profiles at the Plg-glass boundary for elements such as Mg, which is incompatible in Plg, show a positive spike in correspondence with the CBL, which is ~1 μm thick (Fig. 12a). The easiest scenario for modelling the chemical profile of the Plg-CBL-melt system assumes that this system reaches a steady state (e.g. Lucassen et al., 2010). Under these conditions, the concentration of a component across the CBL can be approximated by:

$$C(x,t) = C_2 + (C_1 - C_2)\exp\left(-\frac{v}{D}x\right) \quad (8)$$

where $\boldsymbol{C_1}$ is the concentration of the component at the Plg/CBL interface, $\boldsymbol{C_2}$ is its concentration in the bulk melt/glass far from the CBL, $\boldsymbol{v}$ is the velocity at which the Plg-CBL interface moves into the melt and **D** is the diffusivity in the melt of the component considered. This equation describes diffusion into the half space $x \geq 0$ from a source at $x = 0$, where the strength of the source is related to the difference in element concentrations between the Plg and the melt/glass and the propagation velocity of the crystallization front. The modelled concentration profiles only depend on the ratio $\boldsymbol{k = v/D}$, which can be obtained from a fit of the model curve to the observed concentration data (Lucassen et al., 2009). For such modelling, Mg, Fe and Ti are the most suitable elements. In our study-case, we developed a diffusion chronometry model using the compositional profile of Mg (Fig. 12a) because it best discriminates the glass-CBL-Plg system, where MgO varies from 3.5 wt% in the glass far from the Plg-melt interface to 5–6 wt% within the CBL and then to nearly 0 wt% in the Plg (Fig. 12a). On the other hand, Fe can be incorporated in low amounts (up to 1.0 wt%) in the fast-growing Plg, as shown by both single-spot analyses and chemical profiles (Fig. 11), while Ti concentration in both glass, Plg and CBL are comparatively low. To this end, the data are linearized by rearranging Eq. 8 into:

$$\ln\left(\frac{C_2 - C_{fit}(x,t)}{C_2 - C_1}\right) = -\frac{v}{D_{Mg}}x \quad (9)$$

The diffusion coefficient of Mg in the melt ($\boldsymbol{D_{Mg}}$) was calculated using the equation of Zhang et al. (2010), considering a T interval between 850 and 1100 °C, i.e., a *T* range plausible for erupted trachybasalts at their contact to the air:

$$\ln^{d}_{Mg} = -5.17 - 11.37X_{SA} - 2.16X_{FM} - \frac{10993 + 17839X_{SA}}{T} \quad (10)$$

where X is the cation mole fraction in the melt, X_{FM} = Fe + Mn + Mg, and X_{SA} = Si + Al, and T is the temperature expressed in Kelvin. In accordance to the low amount of H_2O dissolved in the matrix glass (0.07–0.14 wt%) as inferred from FTIR measurements, D_{Mg} was calculated considering anhydrous conditions in the melt. Eq. (9) represents a straight line in $\ln\left(\frac{C_2 - C(x,t)}{C_2 - C_1}\right)$ – *x* space, where $k = \frac{v}{D}$ represents the modulus of the angular coefficient of this line and can be calculated by a linear regression procedure. Solving the equation enables the retrieval of the only unknown *v* which represents the speed at which the interface moved.

Comparing the modelled curve with the measured data profile, both the exponentially fitted curve and the measured profiles align well (Fig. 12b). Assuming an exponentially fitted growth model and Mg diffusivities in the melt D_{Mg} = 1.17 $\mu m^2\ s^{-1}$ (consistent with *T* =

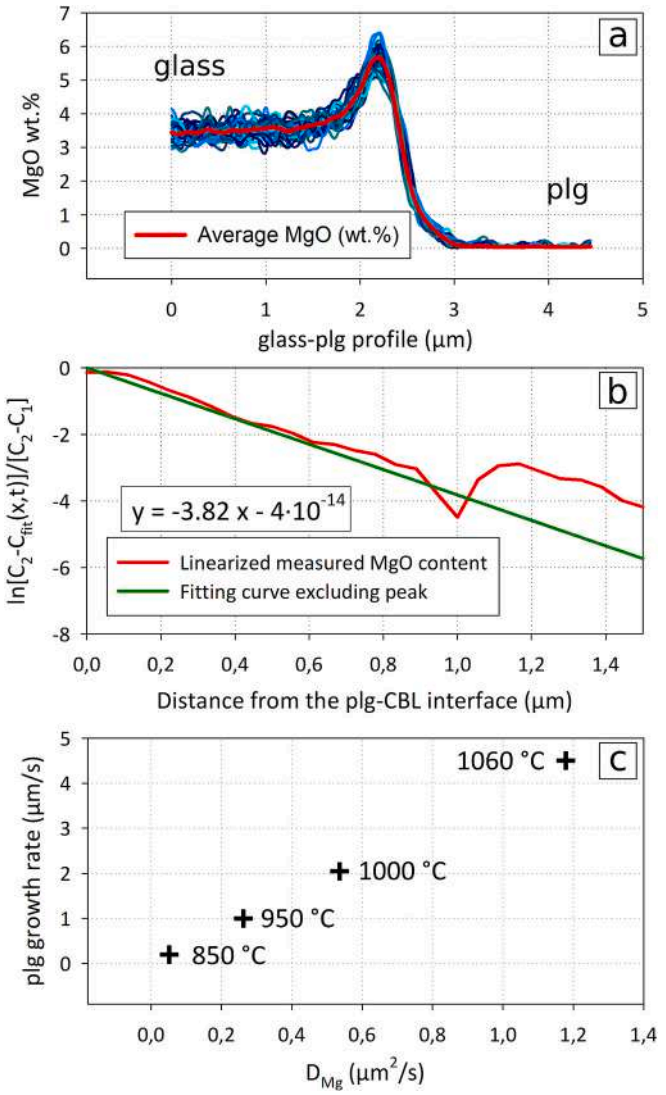

Fig. 12. a) MgO content along the glass-Plg profile showing a peak in correspondence of the CBL before a drop in Plg. b) Eq. 9 represented as a straight line in a $\ln\left(\frac{C_2-C(x,t)}{C_2-C_1}\right)$ – X space; the graph demonstrates that the fitting curve accurately describes the behaviour of the measured MgO profile (also linearized). The graph also includes the equation that fit the linearized profile, with the angular coefficients used to calculate $k = \frac{v}{D} = -3.82$. c) calculated Plg growth rate vs. D_{Mg} at different temperatures.

1060 °C), the estimated growth rate of the Na-rich rim around Plg microlites is 4.5 μm/s (4.5×10^{-4} cm s^{-1}). Considering the lower-end of the temperature range ($T = 850$ °C) and thus adopting $D_{Mg} = 0.051$ μm^2 s^{-1}, the estimated growth rate decreases to 0.2 μm/s (2×10^{-5} cm s^{-1}) (Fig. 12c). It has to be emphasized that the model should be considered as a limit-case scenario and applied with caution. It is possible that a steady-state condition might not have been fully achieved, or it may have been established.

The growth rates calculated for Plg microlites range from 2×10^{-5} cm s^{-1} to 4.5×10^{-4} cm s^{-1}, indicating extremely fast crystallization. Through 4D in situ crystallization experiments in basaltic melts, (Arzilli et al., 2019) obtained very fast growth rates for Plg (from 3×10^{-5} to 1×10^{-4} cm s^{-1}) considering undercooling temperatures ΔT between 60 and 140 °C. Differently from their experiments, where they obtained Plg grains with high morphologic aspect ratio, often showing swallow-tailed textures, our Plg microlites are bulkier and only the ultimate μm-wide Na-rich rims have grown extremely fast and form swallow-tail like features. The main cause of the observed difference could be that in the Bronte lava flow, the relatively more An-rich core regions of the microlites grew slower and in a more isometric shape before the lava we finally exposed to the air. Only the very last moment, when the lava came into contact with the air, a sudden temperature drops close to the quenching temperature, and probably an ultimate episode of H_2O loss, promoted further combined thermal and chemical undercooling of the system, bringing it closer to the nearly anhydrous conditions (measured H_2O in glass = 0.08–0.16 wt%) where the diffusivities of the oxides are slow. Both hypotheses can be valid and not mutually exclusive. In our study case, the most realistic growth rates are the slower ones (2×10^{-5} cm s^{-1}), which likely result from the last crystallization episode taking place at decreasing T (850 °C). Considering 0.5–2 μm thick CBL, this translates into timescales of 2.5 to 10 s for the growth of the rim of Plg microlites in the glass-rich crust of the basaltic flow, in good agreement with what was calculated by D'oriano et al. (2025) for tephra samples from Etna and Stromboli.

The growth rate estimated through this model could be an average of all the growth stages of the Na-rich overgrowth. The listed possibilities correspond with the growth stages described by Welsch et al. (2023). At the very beginning of the temperature drop, the growth rates are probably higher, and consequently CBL could have built up, i.e. the acceleration stage of Welsch et al. (2023). If a steady state was reached the Na-rich rim would be characterized by a linear growth stage (linear growth stage of Welsch et al., 2023), in which the assumptions of the model above are fully valid. The end of crystallization is characterized by a deceleration stage, which may coincide with depletion in components necessary for the crystal to grow (deceleration stages of Welsch et al., 2023). The last stage can also be caused by the formation of a CBL itself. The CBLs surrounding the Plg microlites are not only enriched in oxides such as MgO, FeO, TiO_2, and CaO, which are preferentially partitioned into the melt and consequently repelled from the growing Na-rich rim, but also depleted in slow diffusing oxides such as SiO_2 and Al_2O_3 (Figs. 10e-f), which preferentially partition in the growing crystal (Zhang et al., 2010). If this depletion occurs, the lack of tetrahedra-forming oxides could inhibit or even halt the growth of the Plg crystal itself. This further supports the choice of supercooling conditions, with temperatures <1000 °C, in our case at around 850 °C. Indeed, at higher temperatures (1050 to 1100 °C), the Plg growth rate might increase to sustain the formation of a CBL, but the same problem of depletion in SiO_2 and Al_2O_3 would occur. Although the diffusivities of these elements are higher at high T, they are still lower than the growth rate of Plg, potentially restricting further growth. When the Plg ceases growing, the CBL may temporarily diffuse away from the Plg-melt interface until another growth episode occurs. While this is a plausible scenario, it would likely also produce internal cycling zonation within the Na-rich rim, for which there is currently no chemical and textural evidence (Figs. 10–11).

The obtained timescales indicate that the Na-rich rims of small Plg grains in the groundmass formed right before the final quenching of the lava flow, providing further evidence for the efficiency of Plg crystallization in post-eruptive conditions at Mount Etna (Lanzafame et al., 2013).

5.4. *Significance of the solidification models and future perspectives*

The first outcomes of this study confirmed that even compositionally homogenous individual trachybasaltic lava flows can exhibit significant textural variations at a macro scale (decimetres to metres) along their vertical profile. These variations result from differing crystallization conditions during the *syn-* to post-eruptive stage, emphasizing the importance of adopting appropriate sampling strategies to ensure representativeness. Such variation mostly regards groundmass and vesicles, whereas large phenocrysts display compositional and textural homogeneity along the vertical profile, allowing for reconstruction of the pre-eruptive processes during magma ascent.

The estimated pre-eruptive crystallization conditions of the 1651–1654 eruptive event lie at the lower end of the P-T-X-H_2O range estimated for historic Mount Etna products (Giacomoni et al., 2014, 2021; Mollo et al., 2015b), and differ slightly from those emitted in the 17th century. Indeed, the absence of Ol with Fo > 77 marks a net contrast with the lavas erupted in historic times, which often contain Ol with $Fo_{(84–80)}$ (Giacomoni et al., 2018). The estimated <1080 °C crystallization T of Ol is therefore due to the relatively Fe-rich nature of olivine in the studied samples, suggesting the formation of olivine phenocrysts at shallow conditions. This observation is reinforced by results from Cpx-melt T-P estimates which are comparable with Ol results and restrict the Cpx crystallization conditions to the range of 1069 ± 25 °C and 6.3–2.7 kbar, respectively (21–8 km b.s.l., considering the density model of Corsaro and Pompilio (2004a, 2004b). At these conditions, Ol and Cpx are commonly cotectic on the liquidus for the trachybasaltic compositions of Mount Etna magma but also far from those of parental melts (Lanzafame et al., 2013, 2022; Mollo et al., 2015a, 2015b; Giacomoni et al., 2018). Most of the high-Fo (Fo > 80) Ol likely fractionated from the melt in the deeper portions of the feeding system and the magmatic batch that fed the 1651–1654 eruptive event, while the relatively Fe-rich Ol ($Fo_{80–70}$) in the studied samples formed in the shallower (P < 7 kbar) portion of the feeding system at T lower than those commonly observed in magma erupted from central craters during recent eruptions (Corsaro and Pompilio, 2004a, 2004b; Giacomoni et al., 2018, 2021). Results from the Plg-based hygrometer of Waters and Lange (2015) show that crystal cores formed in a melt with 4 wt% dissolved H_2O, while rims and groundmass crystals formed in a relatively H_2O-poor melt (1 wt% dissolved H_2O) (Fig. 9a). Combined with water exsolution modelling, these data suggest that Plg rims and groundmass crystals formed in the upper portion of the feeding system during/after volatile exsolution (i.e., H_2O, <6 km b.s.l.) and at syn-eruptive conditions.

The investigation on the final stage of crystallization, and in particular the modelled growth rates of Plg at post-eruptive conditions testify very fast solidification, potentially able to grow the observed microlites (up to hundreds of μm in size) in a few minutes. This is apparently in contrast with the well-extended lava flows of the 1651–1654 eruption. A possible explanation for this paradox lies in the architecture of the lava field. The sampling site in this study, a pressure ridge, clearly reveals the formation of a network of lava tunnels that retained high internal temperatures, preventing efficient crystallization. In fact, the calculated Plg growth rates refer only to the crust of the flow, in direct contact with the air and therefore subjected to a very high cooling rate compared to the inner portions. Starting from this, future investigations will focus on better constraining the cooling rates along the vertical profile to the actual growth rates of crystals, and to better quantify the vesiculation process at the post-eruptive stage, to link the crystallization and degassing kinetics to the variation of the rheological properties of the melt. Our findings will contribute to refining predictive models of lava flow behaviour, particularly regarding the links between the viscosity of the lava suspension and its ability to flow, in the context of integrating petrologic real-time monitoring data with risk evaluation during effusive eruptions.

6. Conclusions

The 1651–1654 CE eruption at Mount Etna represented a typical effusive volcanic event occurring in populated areas, a common hazard on volcanoes such as Mount Etna. In this work, a comprehensive study of the crystallization processes occurring in the trachybasaltic melts feeding this eruption, from the magma ascent within the crust to its complete solidification as a lava flow, was carried out by investigating a well-exposed vertical section of a fractured pressure ridge on the pahoehoe lava field. Results advance our knowledge of these physical and chemical processes, but also pose some intriguing questions. The main outcomes of this work are reported in Fig. 13 and summarized as follows:

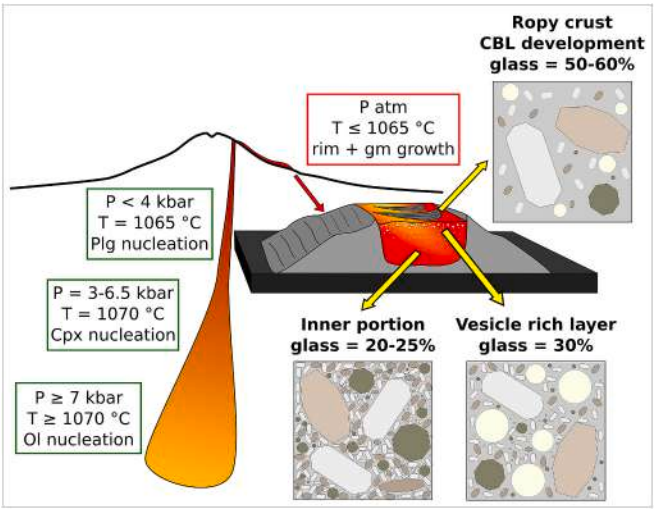

Fig. 13. Schematic model of the pre- to post-eruptive crystallization conditions for the 1651–1654 lavas.

- Before the eruption, the rising magma underwent significant fractionation in a vertically extended polybaric feeding system. Parental magma fractionated most of the high-Fo Ol at P > 7 kbar and phenocrystal Ol and Cpx formed at cotectic conditions at depth between 21 and 8 km b.s.l., at significantly colder conditions than magma commonly erupted from central summit craters. Plg crystallization started in a melt with 4 wt% dissolved H_2O and continued during/after volatile exsolution;

- An initial 4 wt% of dissolved H_2O in the magma started to exsolve only at P < 2.5 kbar, corresponding to ~6 km depth. Degassing continued to the surface during the flow of the lava, as testified by the trend of the small vesicles' distribution and by the chemical analyses on residual glass in the lava samples collected in different portions of the investigated flow unit. The residual amount of H_2O dissolved in the glass after emplacement of the lava flow varies between 0.07 and 0.14 wt%.

- After the emission, the rapid cooling of the flow surface preserved the syn-eruptive solid/liquid proportion of ~40–50 % crystals and ~ 50–60 % melt in the lava at the moment of discharge. This rapid cooling for the reconstruction of the growth history of microlites, detecting and mapping micron-scale chemical boundary layers (CBLs) surrounding Plg and providing a novel perspective on the rapid syn-eruptive crystallization processes. The modelled growth rates are in the range of 4.5 μm/s for T = 1060 °C to 0.2 μm/s for a more conservative value of T = 850 °C.

As shown by the results of this work, the reconstruction of the solidification path in melts feeding effusive eruption is puzzling and must take into account the complex chemical and textural evolution to which magmatic melts are subjected during their journey from deep crust to surface. Determining the melt suspension features at the onset of the subaerial flow, and constraining their evolution with increasing precision, represents an intriguing goal for future research that will be aimed at determining the role of subaerial crystallization and degassing in forecasting the lava flow path, essential for effective monitoring and decision-making in mitigating such events.

CRediT authorship contribution statement

G. Lanzafame: Writing – review & editing, Writing – original draft, Investigation, Data curation, Conceptualization. **S. Peres:** Writing – original draft, Data curation. **F. Casetta:** Writing – original draft, Investigation, Data curation, Conceptualization. **R. Abart:** Writing – original draft, Supervision, Data curation. **M. Prašek:** Writing – original draft, Investigation. **S. Portale:** Writing – original draft, Investigation. **P. P. Giacomoni:** Writing – review & editing, Writing – original draft, Data curation. **E. Libowitzky:** Writing – original draft, Investigation, Data curation. **C. Ferlito:** Writing – original draft, Supervision.

Declaration of competing interest

The authors declare that they have no known competing financial interests or personal relationships that could have appeared to influence the work reported in this paper.

Acknowledgement

We acknowledge the staff of the SYRMEP beamline of Elettra - Sincrotrone Trieste S.C.p.A. for their support during the experiments, Franz Kiraly and Theodoros Ntaflos (University of Vienna, Austria) for their precious assistance during the EPMA analyses and Alexander J. Bolam for the review of the English text. FC acknowledges funding by the Austrian Science Fund (FWF – Der Wissenschaftsfonds) via the ESPRIT Grant number ESP-605. SP acknowledges funding by the Austrian Science Fund (FWF – Der Wissenschaftsfonds) project number P 33227-N (Thomas Griffiths P.I.). We are finally indebted with the Editor Sonia Calvari and two anonymous Reviewers for the precious comments and suggestions that strongly improved the clarity and significance of this study.

Appendix A. Supplementary data

Supplementary data to this article can be found online at https://doi.org/10.1016/j.jvolgeores.2025.108416.

Data availability

Data will be made available on request.

References

Aboulhassan, A., Brun, F., Kourousias, G., Lanzafame, G., Voltolini, M., Contillo, A., Mancini, L., 2022. PyPore3D: an open source software tool for imaging data processing and analysis of porous and multiphase media. J. Imag. 8 (7), 187. https://doi.org/10.3390/jimaging8070187.

Aiuppa, A., Casetta, F., Coltorti, M., Stagno, V., Tamburello, G., 2021. Carbon concentration increases with depth of melting in Earth's upper mantle. Nat. Geosci. 14 (9), 697–703. https://doi.org/10.1038/s41561-021-00797-y.

Aiuppa, A., Lo Bue Trisciuzzi, G., Alparone, S., Bitetto, M., Coltelli, M., Delle Donne, D., Gangi, G., Pecora, E., 2023. A SO2 flux study of the Etna volcano 2020–2021 paroxysmal sequences. Front. Earth Sci. 11, 1115111. https://doi.org/10.3389/feart.2023.1115111.

Anderson, S.W., Smrekar, S.E., Stofan, E.R., 2012. Tumulus development on lava flows: Insights from observations of active tumuli and analysis of formation models. Bull. Volcanol. 74 (4), 931–946. https://doi.org/10.1007/s00445-012-0576-2.

Andronico, D., Lodato, L., 2005. Effusive activity at Mount Etna volcano (Italy) during the 20th century: a contribution to volcanic hazard assessment. Nat. Hazards 36, 407–443. https://doi.org/10.1007/s11069-005-1938-2.

Andronico, D., Branca, S., Calvari, S., Burton, M.R., Caltabiano, T., Corsaro, R.A., Del Carlo, P., Garfi, G., Lodato, L., Miraglia, L., Muré, F., Neri, M., Pecora, E., Pompilio, M., Salerno, G., Spampinato, L., 2005. A multi-disciplinary study of the 2002–03 Etna eruption: insights for a complex plumbing system. Bull. Volcanol. 67 (4), 314–330. https://doi.org/10.1007/s00445–004–0372–8.

Armienti, P., Innocenti, F., Petrini, R., Pompilio, M., Villari, L., 1988. Sub-aphyric alkali basalt from Mt.Etna: inferences on the depth and composition of the source magma. Rend. Soc. It. Mineral. Petrol. 43, 877–891.

Armienti, P., Perinelli, C., Putirka, K.D., 2012. A new model to estimate deep-level magma ascent rates, with applications to Mt. Etna (Sicily, Italy). J. Petrol. 54 (4), 795–813.

Arzilli, F., La Spina, G., Burton, M.R., Polacci, M., Le Gall, N., Hartley, M.E., Di Genova, D., Cai, B., Vo, N.T., Bamber, E.C., Nonni, S., Atwood, R., Llewellin, E.W., Brooker, R.A., Mader, H.M., Lee, P.D., 2019. Magma fragmentation in highly explosive basaltic eruptions induced by rapid crystallization. Nat. Geosci. 12 (12), 1023–1028. https://doi.org/10.1038/s41561-019-0468-6.

Bamber, E.C., La Spina, G., Arzilli, F., Polacci, M., Mancini, L., de' Michieli Vitturi, M., Andronico, D., Corsaro, R.A., Burton, M.R., 2024. Outgassing behaviour during highly explosive basaltic eruptions. Commun. Earth Environ. 5 (1), 3. https://doi.org/10.1038/s43247-023-01182-w.

Beran, A., Koeberl, C., 1997. Water in tektites and impact glasses by fourier-transformed infrared spectrometry. Meteorit. Planet. Sci. 32 (2), 211–216. https://doi.org/10.1111/j.1945-5100.1997.tb01260.x.

Beran, A., Libowitzky, E., 2006. Water in natural mantle minerals II: olivine, garnet and accessory minerals. Rev. Mineral. Geochem. 62 (1), 169–191. https://doi.org/10.2138/rmg.2006.62.8.

Bonechi, B., Polacci, M., Arzilli, F., La Spina, G., Hazemann, J.L., Brooker, R.A., Atwood, R., Marussi, S., Lee, P.D., Wogelius, R.A., Fellowes, J., Burton, M.R., 2024. Direct observation of degassing during decompression of basaltic magma. Sci. Adv. 10 (33), eado2585. https://doi.org/10.1126/sciadv.ado2585.

Branca, S., Abate, T., 2019. Current knowledge of Etna's flank eruptions (Italy) occurring over the past 2500 years. From the iconographies of the XVII century to modern geological cartography. J. Volcanol. Geotherm. Res. 385, 159–178. https://doi.org/10.1016/j.jvolgeores.2017.11.004.

Branca, S., Coltelli, M., de Beni, E., Wijbrans, J., 2008. Geological evolution of Mount Etna volcano (Italy) from earliest products until the first central volcanism (between 500 and 100 ka ago) inferred from geochronological and stratigraphic data. Int. J. Earth Sci. 97 (1), 135–152. https://doi.org/10.1007/s00531-006-0152-0/fulltext.html.

Branca, S., Coltelli, M., Groppelli, G., Lentini, F., 2011. Geological map of Etna volcano, 1:50,000 scale. Italian Journal of Geosciences 130 (3), 265–291.

Brun, F., Massimi, L., Fratini, M., Dreossi, D., Billé, F., Accardo, A., Pugliese, R., Cedola, A., 2017. SYRMEP Tomo Project: a graphical user interface for customizing CT reconstruction workflows. Adv. Struct. Chem. Imaging 3, 1–9. https://doi.org/10.1186/s40679-016-0036-8.

Calvari, S., Pinkerton, H., 1999. Lava tube morphology on Etna and evidence for lava flow emplacement mechanisms. J. Volcanol. Geotherm. Res. 90 (3–4), 263–280. https://doi.org/10.1016/S0377-0273(99)00024-4.

Casetta, F., Giacomoni, P.P., Ferlito, C., Bonadiman, C., Coltorti, M., 2020. The evolution of the mantle source beneath Mt. Etna (Sicily, Italy): from the 600 ka tholeiites to the recent trachybasaltic magmas. Int. Geol. Rev. 62 (3), 338–359. https://doi.org/10.1080/00206814.2019.1610979.

Casetta, F., Ntaflos, T., Aulbach, S., Ashchepkov, I., Faccincani, L., Abart, R., 2025. The chemical stratigraphy of the sub-cratonic lithospheric mantle and its sampling by kimberlites tracked by olivine trace element content. Chem. Geol., 122969 https://doi.org/10.1016/j.chemgeo.2025.122969.

Cashman, K.V., 1993. Relationship between plagioclase crystallization and cooling rate in basaltic melts. Contrib. Mineral. Petrol. 113 (1), 126–142. https://doi.org/10.1007/BF00320836.

Catalano, S., Torrisi, S., Ferlito, C., 2004. The relationship between Late Quaternary deformation and volcanism of Mt. Etna (eastern Sicily): new evidence from the sedimentary substratum in the Catania region. J. Volcanol. Geotherm. Res. 132 (4), 311–334. https://doi.org/10.1016/S0377-0273(03)00433-5.

Chevrel, M.O., Labroquère, J., Harris, A.J., Rowland, S.K., 2018. PyFLOWGO: an open-source platform for simulation of channelized lava thermo-rheological properties. Comput. Geosci. 111, 167–180. https://doi.org/10.1016/j.cageo.2017.11.009.

Cloetens, P., Pateyron-Salomé, M., Buffiere, J.Y., Peix, G., Baruchel, J., Peyrin, F., Schlenker, M., 1997. Observation of microstructure and damage in materials by phase sensitive radiography and tomography. J. Appl. Physiol. 81 (9), 5878–5886. https://doi.org/10.1063/1.364374.

Corsaro, R.A., Pompilio, M., 2004a. Buoyancy-controlled eruption of magmas at Mt Etna. Terra Nova 16 (1), 16–22. https://doi.org/10.1046/j.1365-3121.2003.00520.x.

Corsaro, R.A., Pompilio, M., 2004b. Dynamics of magmas at Mount Etna. Geophys. Monogr. 143, 91–110.

de Beni, E., Wijbrans, J.R., Branca, S., Coltelli, M., Groppelli, G., 2005. New results of Ar-40/Ar-39 dating constrain the timing of transition from fissure-type to central volcanism at Mount Etna (Italy). Terra Nova 17 (3), 292–298. https://doi.org/10.1111/j.1365-3121.2005.00614.x.

D'Orazio, M., Armienti, P., Cerretini, S., 1998. Phenocrysts/matrix trace-element partition coefficients for hawaiite–trachyte lavas from the Ellittico volcanic sequence (Mt. Etna, Sicily, Italy). Mineral. Petrol. 64, 65–88.

D'Oriano, C., Montagna, C., Colucci, S., Del Carlo, P., Brogi, F., Morgavi, D., Musu, A., Arzilli, F., Costa, S., Landi, P., 2025. Fe-rich filamentary textures reveal timescales of magmatic interaction before the onset of high-energy explosive events at basaltic volcanoes. Volcanica 8 (1), 159–174. https://doi.org/10.30909/vol/wytv2139.

Ferlito, C., Lanzafame, G., 2010. The role of supercritical fluids in the potassium enrichment of magmas at Mount Etna volcano (Italy). Lithos 119 (3–4), 642–650. https://doi.org/10.1016/j.lithos.2010.08.006.

Ferlito, C., Coltorti, M., Lanzafame, G., Giacomoni, P.P., 2014. The volatile flushing triggers eruptions at Mount Etna volcano (Italy): evidence from mount etna volcano (Italy). Lithos 184, 447–455. https://doi.org/10.1016/j.lithos.2013.10.030.

Ferlito, C., Bruno, V., Salerno, G., Caltabiano, T., Scandura, D., Mattia, M., Coltorti, M., 2017. Dome-like behaviour at Mt. Etna: the case of the 28 December 2014 South East Crater paroxysm. Sci. Rep. 7 (1), 5361. https://doi.org/10.1038/s41598-017-05318-9.

Gennaro, E., Iacono-Marziano, G., Paonita, A., Rotolo, S.G., Martel, C., Rizzo, A.L., Pichavant, M., Liotta, M., 2019. Melt inclusions track melt evolution and degassing

of Etnean magmas in the last 15 ka. Lithos 324, 716–732. https://doi.org/10.1016/j.lithos.2018.11.023.
Giacomoni, P.P., Ferlito, C., Coltorti, M., Bonadiman, C., Lanzafame, G., 2014. Plagioclase as archive of magma ascent dynamics on "open conduit" volcanoes: the 2001–2006 eruptive period at Mt. Etna. Earth Sci. Rev. 138, 371–393. https://doi.org/10.1016/j.earscirev.2014.06.009.
Giacomoni, P.P., Coltorti, M., Mollo, S., Ferlito, C., Braiato, M., Scarlato, P., 2018. The 2011–2012 paroxysmal eruptions at Mt. Etna volcano: insights on the vertically zoned plumbing system. J. Volcanol. Geotherm. Res. 349, 370–391. https://doi.org/10.1016/j.jvolgeores.2017.11.023.
Giacomoni, P.P., Casetta, F., Valenti, V., Ferlito, C., Lanzafame, G., Nazzari, M., Coltorti, M., 2021. Thermo-barometric constraints on the Mt. Etna 2015 eruptive event. Contrib. Mineral. Petrol. 176, 1–15. https://doi.org/10.1007/s00410-021-01848-8.
Giacomoni, P.P., Masotta, M., Delpech, G., Lanzafame, G., Ferlito, C., Villeneuve, J., Coltorti, M., 2024. Geochemistry and volatile contents of olivine-hosted melt inclusions from Mt. Etna tholeiitic and alkaline magmatism. Contrib. Mineral. Petrol. 179 (5), 47. https://doi.org/10.1007/s00410-024-02116-1.
Giordano, D., Russell, J.K., Dingwell, D.B., 2008. Viscosity of magmatic liquids: a model. Earth Planet. Sci. Lett. 271 (1–4), 123–134. https://doi.org/10.1016/j.epsl.2008.03.038.
Giuliani, L., Iezzi, G., Vetere, F., Behrens, H., Mollo, S., Cauti, F., Ventura, G., Scarlato, P., 2020. Evolution of textures, crystal size distributions and growth rates of plagioclase, clinopyroxene and spinel crystallized at variable cooling rates from a mid-ocean ridge basaltic melt. Earth Sci. Rev. 204, 103165. https://doi.org/10.1016/j.earscirev.2020.103165.
Gregg, T.K.P., 2017. Patterns and processes: subaerial lava flow morphologies: a review. J. Volcanol. Geotherm. Res. 342, 3–12. https://doi.org/10.1016/j.jvolgeores.2017.04.022.
Gualtieri, A.F., Zanni, M., 1998. Quantitative determination of crystalline and amorphous phase in traditional ceramics by combined rietveld-RIR method. Mat. Sci. Forum 278. https://doi.org/10.4028/www.scientific.net/MSF.278-281.834. Trans Tech Publications Ltd.
Harris, A.J., Rowland, S., 2001. FLOWGO: a kinematic thermo-rheological model for lava flowing in a channel. Bull. Volcanol. 63, 20–44. https://doi.org/10.1007/s004450000120.
Harris, A., Bailey, J., Calvari, S., Dehn, J., 2005. Heat loss measured at a lava channel and its implications for down-channel cooling and rheology. In: Manga, M., Ventura, G. (Eds.), Kinematics and Dynamics of Lava Flows, 396. Geol. Soc. Am. Spec. Pap, pp. 125–146. https://doi.org/10.1130/0–8137–2396-5.125 vGSA.
Harris, A.J.L., Rowland, S.K., Villeneuve, N., Thordarson, T., 2017. Pāhoehoe, ʻaʻā, and block lava: an illustrated history of the nomenclature. Bull. Volcanol. 79 (1), 7. https://doi.org/10.1007/s00445-016-1075-7.
Harris, A.J.L., Rowland, S.K., Chevrel, M.O., 2022. The anatomy of a channel-fed ʻaʻā lava flow system. Bull. Volcanol. 84 (7). https://doi.org/10.1007/s00445-022-01578-0.
Herault, A., Vicari, A., Ciraudo, A., Del Negro, C., 2009. Forecasting lava flow hazards during the 2006 Etna eruption: using the MAGFLOW cellular automata model. Comput. Geosci. 35 (5), 1050–1060. https://doi.org/10.1016/j.cageo.2007.10.008.
Herman, G.T., 1980. Image Reconstruction from Projections: The Fundamentals of Computerized. Tomography. Academic Press, New York.
Hon, K., Kauahikaua, J., Denlinger, R., Mackay, K., 1994. Emplacement and inflation of pahoehoe sheet flows: observations and measurements of active lava flows on Kilauea Volcano, Hawaii. Geol. Soc. Am. Bull. 106, 351–370.
Honour, V.C., Holness, M.B., Partridge, J.L., Charlier, B., 2019. Microstructural evolution of silicate immiscible liquids in ferrobasalts. Contrib. Mineral. Petrol. 174, 1–24. https://doi.org/10.1007/s00410-019-1610-6.
Iacovino, K., Till, C.B., 2019. DensityX: A program for calculating the densities of magmatic liquids up to 1,627 C and 30 kbar. Volcanica 2 (1), 1–10. https://doi.org/10.30909/vol.02.01.0110.
Kahl, M., Chakraborty, S., Pompilio, M., Costa, F., 2014. Constraints on the nature and evolution of the magma plumbing system of Mt. Etna volcano (1991-2008) from a combined thermodynamic and kinetic modelling of the compositional record of minerals. J. Petrol. 56 (10), 2025–2068. https://doi.org/10.1093/petrology/egv063.
Kelfoun, K., Vargas, S.V., 2016. In: Harris, A.J.L., De Groeve, T., Garel, F., Carn, S.A. (Eds.), Volcflow Capabilities and Potential Development for the Simulation of Lava Flows. Geol. Soc., London, Spec. Publ, pp. 337–343. https://doi.org/10.1144/SP426.8.
Kolzenburg, S., Chevrel, M.O., Dingwell, D.B., 2022. Magma/suspension rheology. Rev. Mineral. Geochem. 87 (1), 639–720. https://doi.org/10.2138/rmg.2022.87.14.
La Spina, G., Arzilli, F., Burton, M.R., Polacci, M., Clarke, A.B., 2022. Role of volatiles in highly explosive basaltic eruptions. Commun. Earth Environ. 3 (1), 156. https://doi.org/10.1038/s43247-022-00479-6.
Lanzafame, G., Ferlito, C., 2014. Degassing driving crystallization of plagioclase phenocrysts in lava tube stalactites on Mount Etna (Sicily, Italy). Lithos 206, 338–347. https://doi.org/10.1016/j.lithos.2014.08.004.
Lanzafame, G., Mollo, S., Iezzi, G., Ferlito, C., Ventura, G., 2013. Unraveling the solidification path of a pahoehoe "cicirara" lava from Mount Etna volcano. Bull. Volcanol. 75, 1–16. https://doi.org/10.1007/s00445-013-0703-8.
Lanzafame, G., Casetta, F., Giacomoni, P.P., Donato, S., Mancini, L., Coltorti, M., Ntaflos, T., Ferlito, C., 2020. The Skaros effusive sequence at Santorini (Greece): petrological and geochemical constraints on an interplinian cycle. Lithos 362, 105504. https://doi.org/10.1016/j.lithos.2020.105504.
Lanzafame, G., Giacomoni, P.P., Casetta, F., Mancini, L., Iezzi, G., Coltorti, M., Ferlito, C., 2022. Degassing, crystallization and rheology of hawaiitic lava flows: the case of the 1669 AD eruption of Mount Etna (Italy). J. Petrol. 63 (12), egac115. https://doi.org/10.1093/petrology/egac115.
Le Maitre, R.W., Streckeisen, A., Zanettin, B., Le Bas, M.J., Bonin, B., Bateman, P. (Eds.), 2002. Igneous Rocks: A Classification and Glossary of Terms: Recommendations of the International Union of Geological Sciences Subcommission on the Systematics of Igneous Rocks, 2nd ed. Cambridge University Press. https://doi.org/10.1017/CBO9780511535581.
Levich, V.G., 1962. Physicochemical Hydrodynamics. Prentic-Hall, Englewood Cliffs, NJ.
Libowitzky, E., Beran, A., 2006. The structure of hydrous species in nominally anhydrous minerals: information from polarized IR spectroscopy. Rev. Mineral. Geochem. 62 (1), 29–52. https://doi.org/10.2138/rmg.2006.62.2.
Libowitzky, E., Rossman, G.R., 1997. An IR absorption calibration for water in minerals. Am. Mineral. 82 (11–12), 1111–1115. https://doi.org/10.2138/am-1997-11-1208.
Llewellin, E.W., Manga, M., 2005. Bubble suspension rheology and implications for conduit flow. J. Volcanol. Geotherm. Res. 143 (1–3), 205–217. https://doi.org/10.1016/j.jvolgeores.2004.09.018.
Lucassen, F., Dulski, P., Abart, R., Franz, G., Rhede, D., Romer, R.L., 2010. Redistribution of HFSE elements during rutile replacement by titanite. Contrib. Mineral. Petrol. 160, 279–295. https://doi.org/10.1007/s00410-009-0477-3.
Mader, H.M., Llewellin, E.W., Mueller, S.P., 2013. The rheology of two-phase magmas: a review and analysis. J. Volcanol. Geotherm. Res. 257, 135–158. https://doi.org/10.1016/j.jvolgeores.2013.02.014.
Métrich, N., Rutherford, M.J., 1998. Low pressure crystallization paths of H2O-saturated basaltic Hawaiitic melts from Mt Etna: implications for open-system degassing of basaltic volcanoes. Geochim. Cosmochim. Acta 62 (7), 1195–1205. https://doi.org/10.1016/S0016-7037(98)00048-9.
Métrich, N., Allard, P., Spilliaert, N., Andronico, D., Burton, M., 2004. 2001 flank eruption of the alkali-and volatile-rich primitive basalt responsible for Mount Etna's evolution in the last three decades. Earth Planet. Sci. Lett. 228 (1–2), 1–17. https://doi.org/10.1016/j.epsl.2004.09.036.
Mollo, S., Lanzafame, G., Masotta, M., Iezzi, G., Ferlito, C., Scarlato, P., 2011. Cooling history of a dike as revealed by mineral chemistry: a case study from Mt. Etna volcano. Chem. Geol. 288 (1–2), 39–52. https://doi.org/10.1016/j.chemgeo.2011.06.016.
Mollo, S., Misiti, V., Scarlato, P., Soligo, M., 2012. The role of cooling rate in the origin of high temperature phases at the chilled margin of magmatic intrusions. Chem. Geol. 322, 28–46. https://doi.org/10.1016/j.chemgeo.2012.05.029.
Mollo, S., Blundy, J.D., Iezzi, G., Scarlato, P., Langone, A., 2013a. The partitioning of trace elements between clinopyroxene and trachybasaltic melt during rapid cooling and crystal growth. Contrib. Mineral. Petrol. 166, 1633–1654. https://doi.org/10.1007/s00410-013-0946-6.
Mollo, S., Scarlato, P., Lanzafame, G., Ferlito, C., 2013b. Deciphering lava flow post-eruption differentiation processes by means of geochemical and isotopic variations: a case study from Mt. Etna volcano. Lithos 162, 115–127. https://doi.org/10.1016/j.lithos.2012.12.020.
Mollo, S., Giacomoni, P.P., Andronico, D., Scarlato, P., 2015a. Clinopyroxene and titanomagnetite cation redistributions at Mt. Etna volcano (Sicily, Italy): footprints of the final solidification history of lava fountains and lava flows. Chem. Geol. 406, 45–54. https://doi.org/10.1016/j.chemgeo.2015.04.017.
Mollo, S., Giacomoni, P.P., Coltorti, M., Ferlito, C., Iezzi, G., Scarlato, P., 2015b. Reconstruction of magmatic variables governing recent Etnean eruptions: constraints from mineral chemistry and P–T–fO_2–H_2O modeling. Lithos 212, 311–320. https://doi.org/10.1016/j.lithos.2014.11.020.
Mollo, S., Blundy, J.D., Giacomoni, P., Nazzari, M., Scarlato, P., Coltorti, M., Langone, A., Andronico, D., 2017. Clinopyroxene-melt element partitioning during interaction between trachybasaltic magma and siliceous crust: clues from quartzite enclaves at Mt. Etna volcano. Lithos 284, 447–461. https://doi.org/10.1016/j.lithos.2017.05.003.
Monaco, C., De Guidi, G., Ferlito, C., 2010. The morphotectonic map of Mt. Etna. Ital. J. Geosci. 129 (3), 408–428. https://doi.org/10.3301/IJG.2010.11.
Namiki, A., Saito, K., Okumura, A., Hoshino, M., Uesugi, K., Tsukada, K., Takagi, N., Manga, M., 2025. Crystal-rich magma is solid-like and liquefies when deformed. J. Geophys. Res. Solid Earth 130 (3), e2024JB030483. https://doi.org/10.1029/2024JB030483.
Nicotra, E., Viccaro, M., 2012. Unusual magma storage conditions at Mt. Etna (Southern Italy) as evidenced by plagioclase megacryst-bearing lavas: implications for the plumbing system geometry and summit caldera collapse. Bull. Volcanol. 74, 795–815. https://doi.org/10.1007/s00445-011-0566-9.
Paganin, D., Mayo, S.C., Gureyev, T.E., Miller, P.R., Wilkins, S.W., 2002. Simultaneous phase and amplitude extraction from a single defocused image of a homogeneous object. J. Microsc. 206 (1), 33–40. https://doi.org/10.1046/j.1365-2818.2002.01010.x.
Pichavant, M., Di Carlo, I., Pompilio, M., Le Gall, N., 2022. Timescales and mechanisms of paroxysm initiation at Stromboli volcano, Aeolian Islands, Italy. Bull. Volcanol. 84 (4), 36. https://doi.org/10.1007/s00445-022-01545-9.
Polacci, M., Papale, P., 1997. The evolution of lava flows from ephemeral vents at Mount Etna: insights from vesicle distribution and morphological studies. J. Volcanol. Geotherm. Res. 76, 1–17.
Pouchou, J.L., Pichoir, F., 1991. Quantitative analysis of homogeneous or stratified microvolumes applying the model "PAP". In: Electron Probe Quantitation. Springer US, Boston, MA, pp. 31–75. https://doi.org/10.1007/978-1-4899-2617-3_4.
Putirka, K.D., 2008. Thermometers and barometers for volcanic systems. Rev. Mineral. Geochem. 69 (1), 61–120. https://doi.org/10.2138/rmg.2008.69.3.
Putirka, K., Ryerson, F.J., Mikaelian, H., 2003. New igneous thermobarometers for mafic and evolved lava compositions, based on clinopyroxene+ liquid equilibria. Am. Mineral. 88, 1542–1554.

Rittmann, A., 1965. Notizie sull'Etna. Suppl. Nuovo Cimento 3 (I), 1117–1123.
Robert, B., Harris, A., Gurioli, L., Médard, E., Sehlke, A., Whittington, A., 2014. Textural and rheological evolution of basalt flowing down a lava channel. Bull. Volcanol. 76 (6), 1–21. https://doi.org/10.1007/s00445-014-0824-8.
Roeder, P.L., Emslie, R., 1970. Olivine-liquid equilibrium. Contrib. Mineral. Petrol. 29 (4), 275–289. https://doi.org/10.1007/BF00371276.
Rossman, G.R., 2006. Analytical methods for measuring water in nominally anhydrous minerals. Rev. Mineral. Geochem. 62 (1), 1–28. https://doi.org/10.2138/rmg.2006.62.1.
Rust, A.C., Manga, M., 2002. Effects of bubble deformation on the viscosity of dilute suspensions. J. Non-Newton. Fluid Mech. 104 (1), 53–63. https://doi.org/10.1016/S0377-0257(02)00013-7.
Shea, T., Hammer, J.E., 2013. Kinetics of cooling-and decompression-induced crystallization in hydrous mafic-intermediate magmas. J. Volcanol. Geotherm. Res. 260, 127–145. https://doi.org/10.1016/j.jvolgeores.2013.04.018.
Spilliaert, N., Allard, P., Métrich, N., Sobolev, A.V., 2006. Melt inclusion record of the conditions of ascent, degassing, and extrusion of volatile-rich alkali basalt during the powerful 2002 flank eruption of Mount Etna (Italy). J. Geophys. Res. Solid Earth 111 (B4). https://doi.org/10.1029/2005JB003934.
Spina, A.L., Burton, M., Salerno, G., Caltabiano, T., 2023. Insights into magma dynamics at Etna (Sicily) from SO2 and HCl fluxes during the 2008–2009 eruption. Geology 51 (5), 419–423. https://doi.org/10.1130/G50707.1.
Tanguy, J.C., Condomines, M., Kieffer, G., 1997. Evolution of the Mount Etna magma: constraints on the present feeding system and eruptive mechanism. J. Volcanol. Geotherm. Res. 75 (3–4), 221–250. https://doi.org/10.1016/S0377-0273(96)00065-0.
Trigila, R., Spera, F.J., Aurisicchio, C., 1990. The 1983 Mount Etna eruption: thermochemical and dynamical inferences. Contrib. Mineral. Petrol. 104, 594–608.
Troll, V.R., Aulinas, M., Carracedo, J.C., Geiger, H., Perez-Torrado, F.J., Soler, V., Deegan, F.M., Bloszies, C., Weis, F., Albert, H., Gisbert, G., Day, J.M.D., Rodriguez-Gonzalez, A., Gazel, E., Dayton, K., 2024. The 2021 La Palma eruption: social dilemmas resulting from life close to an active volcano. Geol. Today 40 (3), 96–111. https://doi.org/10.1111/gto.12472.
Truby, J.M., Mueller, S.P., Llewellin, E.W., Mader, H.M., 2015. The rheology of three-phase suspensions at low bubble capillary number. Proc. R. Soc. Lond. A. Math. Phys. Eng. Sci. 471 (2173), 20140557. https://doi.org/10.1098/rspa.2014.0557.
Vetere, F., Mollo, S., Giacomoni, P.P., Iezzi, G., Coltorti, M., Ferlito, C., Holtz, F., Perugini, D., Scarlato, P., 2015. Experimental constraints on the origin of pahoehoe "cicirara" lavas at Mt. Etna Volcano (Sicily, Italy). Bull. Volcanol. 77, 1–18. https://doi.org/10.1007/s00445-015-0931-1.
Vona, A., Romano, C., Dingwell, D.B., Giordano, D., 2011. The rheology of crystal-bearing basaltic magmas from Stromboli and Etna. Geochim. Cosmochim. Acta 75 (11), 3214–3236. https://doi.org/10.1016/j.gca.2011.03.031.
Walker, G.P.L., 1991. Structure, and origin by injection under surface crust of tumuli, "lava rises," "lava-rise pits" and "lava inflation clefts" in Hawaii. Bull. Volcanol. 53 (7), 546–558.
Waters, L.E., Lange, R.A., 2015. An updated calibration of the plagioclase-liquid hygrometer-thermometer applicable to basalts through rhyolites. Am. Mineral. 100 (10), 2172–2184. https://doi.org/10.2138/am-2015-5232.
Welsch, B., Faure, F., First, E.C., 2023. Reappraising crystallization kinetics with overgrowth chronometry: an in situ study of olivine growth velocities. J. Petrol. 64, 1–29. https://doi.org/10.1093/petrology/egad055.
Wieser, P.E., Kent, A.J.R., Till, C.B., Donovan, J., Neave, D.A., Blatter, D.L., Krawczynski, M.J., 2023a. Barometers behaving badly I: assessing the influence of analytical and experimental uncertainty on Clinopyroxene thermobarometry calculations at crustal conditions. J. Petrol. 64 (2), 1–27. https://doi.org/10.1093/petrology/egac126.
Wieser, P.E., Kent, A.J.R., Till, C.B., 2023b. Barometers behaving badly II: a critical evaluation of Cpx-only and Cpx-Liq thermobarometry in variably-hydrous arc magmas. J. Petrol. 64 (8), 1–25. https://doi.org/10.1093/petrology/egad050.
Witham, F., Blundy, J., Kohn, S.C., Lesne, P., Dixon, J., Churakov, S.V., Botcharnikov, R., 2012. SolEx: a model for mixed COHSCl-volatile solubilities and exsolved gas compositions in basalt. Comput. Geosci. 45, 87–97. https://doi.org/10.1016/j.cageo.2011.09.021.
Zellmer, G.F., Sakamoto, N., Hwang, S.L., Matsuda, N., Iizuka, Y., Moebis, A., Yurimoto, H., 2016. Inferring the effects of compositional boundary layers on crystal nucleation, growth textures, and mineral chemistry in natural volcanic tephras through submicron-resolution imaging. Front. Earth Sci. 4, 88. https://doi.org/10.3389/feart.2016.00088.
Zhang, Y., Ni, H., Chen, Y., 2010. Diffusion data in silicate melts. Rev. Mineral. Geochem. 72 (1), 311–408. https://doi.org/10.2138/rmg.2010.72.8.